Energetic motions in turbulent partially-filled pipe flow

Henry C.-H. Ng,[1, a)] Emile Collignon,[1, 2] Robert J. Poole,[1] and David J. C. Dennis[1]
[1)]*School of Engineering, University of Liverpool, Liverpool L69 3GH, UK*
[2)]*Département de Mathématique et Méchanique, ENSEIRB-MATMECA, 33400, Talence, France*

Turbulent partially-filled pipe flow was investigated using Stereoscopic Particle Imaging Velocimetry (S-PIV) in the cross-stream plane for a range of flow depths at a nominally constant Reynolds number of 30,000 (based on bulk velocity and hydraulic diameter). Unlike full pipe flow, which is axisymmetric, the turbulent kinetic energy exhibits significant azimuthal (and radial) variation. Proper orthogonal decomposition (POD) of the fluctuating velocity field indicates that the leading order POD modes occupy the "corners" where the free surface meets the pipe wall and that these modes, which are closely linked to the instantaneous cellular structure, contribute nearly a quarter of the overall turbulent kinetic energy. Spatial distributions of the large- and very-large-scale motions (LSMs/VLSMs) estimated from pseudo-instantaneous three-dimensional velocity fields reveal a preference for the sides (in close proximity to the free surface) and bottom quadrant of the pipe. That the LSMs and VLSMs are shown to populate a region spanning the width of the free surface, as well as the corners, strongly suggests that there is a dynamical connection between LSMs/VLSMs and the instantaneous cellular structures in turbulent partially-filled pipe flow which can explain the spatial redistribution of the turbulent kinetic energy.

I. INTRODUCTION

The flow in partially-filled pipes has received far less attention than canonical, full bore, pipe-flow. Partially-filled pipe flow, however, also has several important applications, such as the transport of particulates in solution (an application of interest to the decommissioning of nuclear power plants) and many hydraulic applications such as subsurface drainage and the transport of wastewater. It was only relatively recently that Guo and Meroney [1] reported an analytical solution for laminar pipe flow running partially full. As yet, numerical studies of this problem only deal with laminar flow, for example, Davis and Mai [2] and Ng, Lawrence, and Hewitt [3]. Measurements of the velocity distribution in turbulent flow for smooth walled circular pipes running partially full are very sparse, with notable examples reported by Knight and Sterling [4] and Yoon, Sung, and Lee [5].

In a recent work, Ng *et al.* [6], we used two-dimensional, three-component (2D-3C) high-speed stereoscopic particle imaging velocimetry to detail the velocity field of partially-filled pipes for both the laminar *and* turbulent flow regimes. We showed that the measured velocity distribution in laminar flow is in excellent agreement with the analytical solution of Guo and Meroney [1] and that the so-called "velocity dip" only occurs in laminar flow at fill depths $d/D \gtrsim 90\%$, where d is flow depth measured at the pipe vertical bisector and D is pipe diameter. Measurements of the velocity field in turbulent flow revealed the velocity dip occurred for fill depths as low as $d/D = 44\%$ and was accompanied by a mean secondary flow, which remained close to the free surface for flow depths up to $d/D = 80\%$. Using two-point spatio-temporal correlations of the streamwise velocity fluctuations we showed that the presence of the mean secondary flow had a significant effect on the large-scale turbulent flow structures in relation to those in canonical pipe flow.

[a)]Electronic mail: hchng@liverpool.ac.uk

The large-scale structures in wall-bounded turbulent flows have received much attention in recent years. These elongated structural elements are often termed large-scale and very-large-scale motions (LSM/VLSM) in channel and pipe flow and "Superstructures" in boundary-layer flows. Kim and Adrian [7] first inferred the existence of these elongated structures from the bi-modal energy distribution in the streamwise velocity spectrum acquired using single-point hot-wire measurements in turbulent pipe flow. They identified spectral peaks at wavelengths λ_x non-dimensionalised by pipe radii R of $1 \lesssim \lambda_x/R \lesssim 3$ and $12 \lesssim \lambda_x/R \lesssim 14$ as the signatures of the LSMs and VLSMs, respectively. Hutchins and Marusic [8] showed that structurally similar events existed in turbulent boundary layers and that whilst the streamwise energy distribution peaked at a wavelength of $\lambda_x/\delta \approx 6$ (δ being the boundary-layer thickness), traces of streamwise velocity fluctuation obtained using a hot-wire rake showed evidence of pseudo-instantaneous structures with lengths of up to $O(20\delta)$. Many works, both experimental and numerical, have since furthered our understanding of those long coherent motions in pipes and channels[9–18] and boundary layers[19–21] and have highlighted the importance of the LSMs and VLSMs in relation to turbulent kinetic energy and Reynolds shear stress production and transport. Studies linking the existence of LSMs and VLSMs to the instantaeous cellular structure in open channel flow over both smooth and rough surfaces have been gaining traction in recent years[22–27] as the similarities between the large scale structures that populate canonical wall-bounded turbulent flows and the coherent structure in open channel flows[28,29] and free surface turbulence[30–32], such as the "upwellings", "downdrafts", "whirlpools"[33], aforementioned instantaneous cellular structure[34] and mean secondary flows, are difficult to ignore. Turbulent partially-filled pipe flow shares many elements of open channel flows and canonical pipe flows and our previous work has shown that the coherent structures in both aforementioned flow configurations co-exist in partially-filled pipe flow[6].

In the current study we aim to explore the influence of the LSMs and VLSMs on the standout features of turbulent

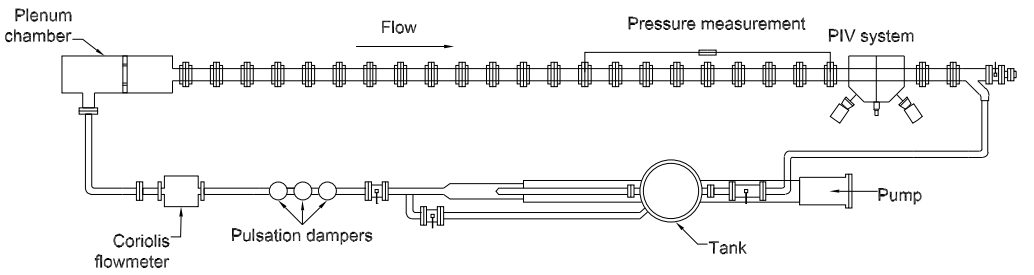

FIG. 1. Schematic of VLSPF facility.

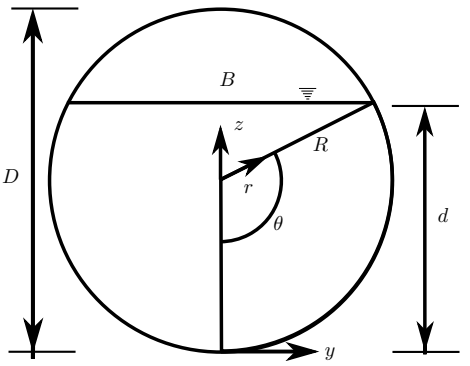

FIG. 2. Cross-section of pipe showing definitions of depth and free surface width.

partially-filled pipes, such as the velocity "dip", the associated mean secondary flow and the preferential spatial distribution of the turbulent kinetic energy. The remainder of the manuscript is organised as follows: the experimental setup and database is introduced in §II and then the mean velocity flow field and mean turbulence statistics are briefly recapped in §III. In §IV, we use proper orthogonal decomposition (POD) to identify, visualize and deduce the makeup and *locations* of the large-scale energy containing motions and also study the characteristics of a POD-filtered, low-order representation of the velocity field. We then identify and extract large- and very-large-scale motions from pseudo-instantaneous velocity fields and determine their characteristics in §V before presenting the conclusions in §VI.

II. EXPERIMENTAL SETUP & S-PIV DATABASE

High-speed Stereoscopic PIV (S-PIV) data reported in Ng *et al.*[6] is examined here. These data were obtained in the Very Large Scale Pipe Flow (VLSPF) facility at the University of Liverpool. The VLSPF facility has a working section length of $L = 23.3$m made up of precision-bore borosilicate glass tubes of $D = 100 \pm 0.4$mm and matching machined-to-fit stainless steel flanges. The flow loop consists of a 500 litre header tank, which feeds a progressive cavity pump (*Mono* Type-101). Fluid is then pumped through a set of three pulsation dampeners and passes through a Coriolis-type mass flow meter (*Endress and Hauser Promass 63*) before entering a plenum chamber where the flow is fully reversed to remove residual swirl. Flow then travels through the working section and is returned to the header tank via a flexible rubber hose. A schematic of the rig is shown in figure 1. The facility was not modified to run in partially-filled configuration with a detailed description of the operating protocol used to achieve partially-filled flow provided in Ng *et al.*[6] and omitted here for brevity. The facility is the same rig used for the full-bore pipe-flow measurements recently reported in Owolabi, Dennis, and Poole[36] and Wen *et al.*[37] (essentially an extended version of the facility originally used by Escudier, Presti, and Smith[38]).

The S-PIV data was collected in the radial-azimuthal plane at an axial location of $x/D \approx 220$ from the inlet. Particle images of the flow were acquired via a pair of *Nikon Micro-Nikkor* 60mm camera lenses set to f-4.0 attached to two *Phantom Miro M110* high-speed CMOS cameras using Scheimpflug mounts that facilitated stereoscopic imaging. The cameras have sensor resolution of 1280×800 pixels, a 12-bit dynamic range and at full resolution are capable of capturing images at a maximum repetition rate of $f = 1600$Hz. The measurement plane was viewed through a prism filled with the same working fluid as the pipe facility and the cameras were synchronised with the laser light pulses emitted from an Nd:YAG laser (*Lee Laser LDP-100MQG DUAL*). The flow was seeded with silver-coated hollow glass spheres with an average diameter of 10μm and a custom made two-level calibration target made up of a lattice of dots of known spacing with a 3mm axial offset is imaged prior to the flow measurements. The reconstruction of the three-component vector fields from the calibration and particle images was performed using *Dantec Dynamics DynamicStudio 2015a* with a final interrogation window size of 32×32 pixels and 50% overlap which yielded an approximate measurement resolution of $l = 2$mm. The S-PIV data were acquired at both low and high repetition rates. The former done so that a sizable number of independent vector fields facilitated well converged time-

d/D[%]	Re_H	Re_{EQ}	Fr	U_b[mm/s]	Vector fields per sec.	PIV realisations	TU_b/R
44	29,300	20,700	0.52	311	1	6150	38253
52	30,100	21,300	0.43	289	1	6000	34680
62	31,000	22,300	0.36	268	2	10250	27470
70	30,300	22,500	0.30	252	2.5	12300	24797
80	28,500	22,100	0.25	234	2.5	12300	23026
44	29,400	20,800	0.53	311	382	29725	484
62	31,300	22,500	0.37	273	291	29725	558
80	28,700	22,100	0.25	236	255	25625	474
†100	35,000	35,000	N/A	350	500	21268	512.4

TABLE I. Experimental conditions for turbulent flow velocity measurements. †Data from Dennis and Sogaro [35].

averaged statistics and the latter to obtain a spatio-temporal 3D view of the flow field and large structures. The high repetition rate data were collected in discrete blocks of 1025 PIV image pairs with a minimum of 25 blocks per flow depth investigated.

Data were acquired at a nominally constant Reynolds number of $Re_H = D_H U_b/\nu \approx 30{,}000 \pm 5\%$ for flow depths ranging between $44\% \leq d/D \leq 80\%$ where D_H is the hydraulic diameter, U_b bulk velocity, ν kinematic viscosity, d the flow depth measured along the pipe vertical bisector and D is the pipe diameter. The hydraulic diameter $D_H = 4A/P_w$ is a function of flow cross-sectional area (A) and wetted perimeter (P_w). In a partially-filled pipe (with circular cross-section), $A = R^2(\theta - \sin\theta\cos\theta)$ and $P_w = 2R\theta$, where $\theta = \cos^{-1}((R-d)/R)$ is the angle subtended by the arc between the bottom-dead-center of the pipe and the location where the free surface meets the pipe wall. A partially-filled pipe flow has a free surface and so the Froude number $Fr = U_b/\sqrt{g \times D_m}$ becomes important. Here g is gravitational acceleration and $D_m = A/B$ the hydraulic mean depth which is dependent on free surface width B. In a partially-filled pipe with circular cross section, $B = 2R\sin\theta$. In this paper x, y and z refer to the streamwise, spanwise and vertical directions with respect to the pipe vertical bisector, with u, v and w the respective velocity components in Cartesian co-ordinates. Radial (r) and azimuthal (θ) directions are defined from the pipe centre axis. Figure 2 provides definitions of geometric parameters and table I summarizes the relevant experimental conditions and S-PIV parameters.

III. MEAN FLOW

The time-averaged mean flow field was previously described in detail Ng *et al.* [6] so here we only provide a short description of the salient features for completeness. Figure 3 displays contours of the time-averaged streamwise velocity distribution normalised with bulk velocity U/U_b, with corresponding in-plane velocity vectors superimposed. We have exploited the symmetry of the flow about the vertical bisector to improve the statistics. The maximum streamwise velocity appears below the free surface for the five flow depths tested (although only three flow depths are shown in figure 3 for brevity), representative of the so-called "velocity dip" phenomenon. The contours of U/U_b are distorted (relative to full pipe flow) by the presence of a mean secondary flow which consists of a pair of large-scale counter-rotating rollers, each filling the half-width of the pipe. The secondary flow (observed for all flow depths tested) is the so-called Prandtl secondary flow of the second kind[39] driven by turbulence anisotropy and spatial gradients of the Reynolds shear stresses[40] due to the breaking of azimuthal symmetry by introducing the free surface.

Profiles of mean streamwise velocity along the pipe vertical bisector for flow depths between $44\% \leq d/D \leq 80\%$ are plotted together in figure 4. Unlike one might do for canonical pipe flow, we were not able to determine friction velocity U_τ from pressure-drop measurements (as the pressure taps in the VLSPF were located near the top-dead-center of the pipe) and as our S-PIV measurements cannot reliably resolve velocities in the viscous sublayer we have refrained from presenting velocity data scaled using wall variables and only present data scaled with outer variables. Since partially-filled pipe flow does not have a single natural outer length scale (which, for a full pipe is simply radius R or diameter D), the velocity profiles presented in figure 4 are scaled using length scales of D, d and D_H and velocity scales of U_b and U_{max} (the latter representing maximum streamwise velocity), respectively. The full pipe flow velocity profile taken from data acquired in the VLSPF facility by Dennis and Sogaro [35] is included for comparison. When scaling with D and U_b (figure 4a), there is good collapse near the "lower" wall for all cases (including full pipe flow) revealing that up to the location of U_{max} in a partially-filled pipe flow, the behaviour is very similar to that of full pipe flow. When rescaled with d and U_b (figure 4b) we see that the proportion of the velocity profile above the mean velocity, i.e. $U/U_b > 1$, increases with increasing flow depth and that when z/d approaches unity, the mean velocity gradient tends to zero for the partially-filled pipe. Finally, when scaling with D_H (commonly used in compound open-channel flows) and U_{max}, the velocity profiles in partially-filled pipe flow collapse well, but do not tend to full pipe flow. Interestingly, with this scaling the location of U_{max} appears constant at $z/D_H \approx 0.3$. Regardless of the length and velocity scales used, we note that U_{max} occurs below the free surface (i.e ."velocity dip" phenomenon) for all flow depths tested and

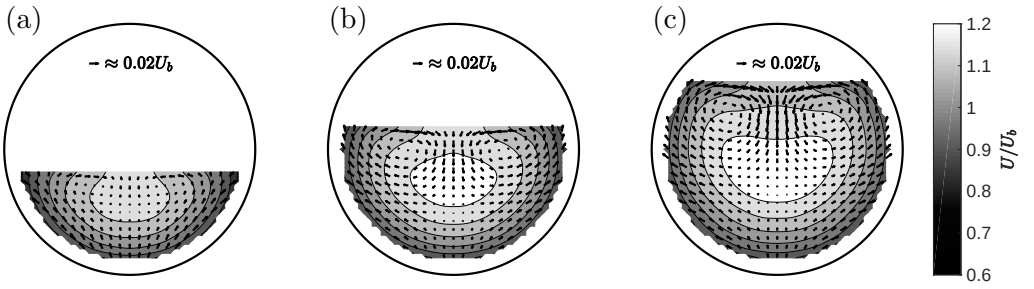

FIG. 3. Contours of time-averaged streamwise velocity normalised with bulk velocity U/U_b for flow depths: (a) $d/D = 44\%$, (b) $d/D = 62\%$ and (c) $d/D = 80\%$ at $Re_H \approx 30,000$. The time-averaged in-plane velocity vectors are superimposed.

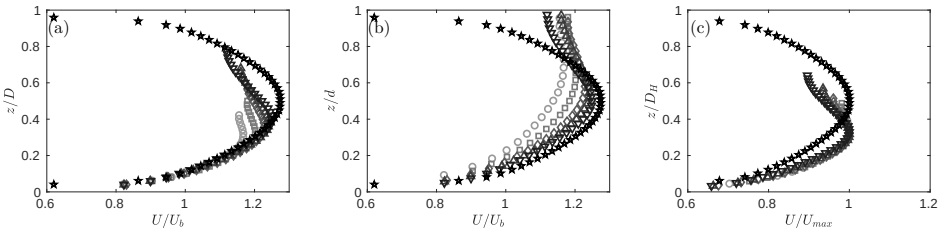

FIG. 4. Mean streamwise velocity along vertical bisector scaled with (a) pipe diameter D and bulk velocity U_b, (b) flow depth d and bulk velocity U_b and (c) hydraulic diameter D_H and maximum streamwise velocity U_{max}. ($\circ$): $d/D = 44\%$, ($\square$): $d/D = 52\%$, ($\diamond$): $d/D = 62\%$, ($\triangle$): $d/D = 70\%$, ($\triangledown$): $d = 80\%$ and ($\star$): $d/D = 100\%$. Grayscale shading increases with increasing flow depth.

that the mean velocity gradient when approaching the free surface approaches zero implying that, at least along the vertical bisector, we have a "true" stress free surface at the air/fluid interface in our pipe working section.

In figure 5 we show filled contours of the TKE distribution across the r-θ plane of the pipe, with contour lines of mean streamwise velocity superimposed (again flow depths $d/D = 52\%$ and 70% were omitted for brevity). The distribution of $\overline{u^2}$ (previously shown in Ng *et al.* [6]) is nearly identical to that of the TKE distribution indicating that $\overline{u^2}$ remains the dominant contributor to TKE, hence contours of $\overline{u^2}$ are not shown here. Unlike full pipe flow, which is axisymmetric, the TKE distribution exhibits pronounced azimuthal variation. We observe increased activity in the bottom and "sides" of the pipe and decreased TKE along approximately the $\pm 45^\circ$ bisectors. It is thought that the preferential distribution of the TKE (and $\overline{u^2}$) is impacted by the presence of the mean secondary motion.

Figure 6 shows profiles of turbulence statistics (normalised with bulk velocity) taken along the pipe vertical bisector scaled with the flow depth d. Interestingly, turbulent kinetic energy (TKE), streamwise Reynolds normal stress ($\overline{u^2}$), as well as, the Reynolds shear stress ($-\overline{uw}$), all peak at approximately $z/d = 0.2$ which could be thought of as the edge of the outer region in canonical pipe flow (where d here would be analogous to pipe radius R). Beyond $z/d \approx 0.2$ both $\overline{u^2}$ and TKE appear to decrease linearly with depth up to $z/d \approx 0.5$ which coincides with the location of U_{max}. For $z/d > 0.5$, a peculiar trend emerges. Up to a flow depth of $d/D = 52\%$, $\overline{u^2}$ and TKE remain constant from $z/d = 0.5$ until the free surface. For flow depths greater than $d/D = 52\%$, both $\overline{u^2}$ and TKE increase between $z/d = 0.5$ and the free surface, the magnitude of which is increasing with increasing flow depth. Profiles of $-\overline{uw}$ (figure 6c) also all peak at approximately $z/d = 0.2$ and then begin to decrease with increasing z/d. For all flow depths except $d/D = 44\%$, $-\overline{uw}$ changes sign between $0.4 < z/d < 0.6$ which coincides with the sign change in the mean streamwise velocity gradient. Between $0.5 \lesssim z/d \lesssim 0.75$, $-\overline{uw}$ becomes increasingly negative with the magnitude of the minimum value increasing with increasing flow depth, i.e. increasing from $d/D = 44\%$ to $d/D = 80\%$. With z/d very close to unity, $-\overline{uw}$ returns to zero as expected. That the TKE and Reynolds stress distributions are different to canonical pipe flow is not surprising: by reducing flow depth and introducing a free surface, the boundary condition for the upper part of the flow changes from no-slip wall to that of no mean shear. When z/d tends to unity, turbulence production approaches zero due to the lack of mean shear (at least along the vertical bisector) leading to the reduction in Reynolds shear and normal stresses, as well as TKE in the upper part of the flow near the free surface.

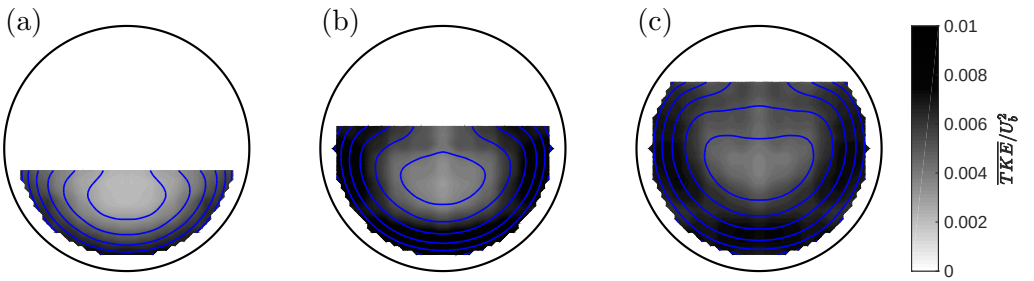

FIG. 5. Contours of time-averaged turbulent kinetic energy (TKE) normalised with bulk velocity $\overline{TKE}/U_b^2$ for flow depths: (a) $d/D = 44\%$, (b) $d/D = 62\%$ and (c) $d/D = 80\%$ at $Re_H \approx 30,000$. Solid blue lines represent the corresponding mean streamwise velocity contour distribution.

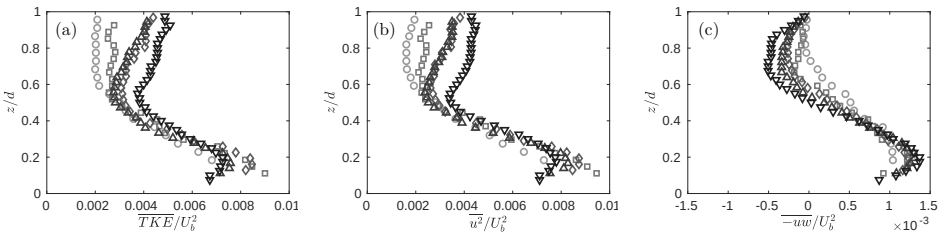

FIG. 6. Profiles of (a) turbulent kinetic energy $\overline{TKE^2}/U_b^2$, (b) $\overline{u^2}/U_b^2$ and (c) Reynolds shear stress $-\overline{uw}/U_b^2$ along vertical bisector plotted as a function of flow depth. ($\circ$): $d/D = 44\%$, ($\square$): $d/D = 52\%$, ($\diamond$): $d/D = 62\%$, ($\triangle$): $d/D = 70\%$ and ($\triangledown$): $d/D = 80\%$. Grayscale shading increases with increasing flow depth.

IV. PROPER ORTHOGONAL DECOMPOSITION

The proper orthogonal decomposition (POD) is a commonly-used modal analysis technique to visualize coherent features in turbulent flows[41–46] and has recently been successfully applied to elucidate the large-scale structures in fully-developed turbulent canonical pipe flows[14,47–50]. When applied to the fluctuating velocity field, POD modes are obtained by maximizing the turbulent kinetic energy over the data set. The decomposition can be written as

$$\mathbf{u}(x,y,z,t) = \sum_{i=1}^{N} a_i(t)\Phi_i(x,y,z) \tag{1}$$

where $\mathbf{u}(u,v,w)$ is the velocity fluctuation vector, Φ_i is the eigenmode of the i^{th} mode, $a_i(t)$ is the mode's temporal (or random) co-efficient and N is the total number of modes.

The fluctuating velocity components (u, v and w), acquired in Cartesian co-ordinates were first interpolated onto a new mesh with bi-polar coordinates (ξ,η) to remove the points outside the physical flow domain while arranging the velocity components in a non-sparse rectangular matrix. The bipolar co-ordinate system for partially-filled pipe flow was given by Guo and Meroney [1] and its relationship to Cartesian coordinates is given by

$$\frac{y}{R} = \frac{\sin\theta \sinh\xi}{\cosh\xi - \cos\eta}, \tag{2}$$

and

$$\frac{z}{R} = \frac{\sin\theta \sin\eta}{\cosh\xi - \cos\eta}. \tag{3}$$

The increments of ξ and η were chosen such that the maximum spacing of the bi-polar grid matched the resolution of the acquired data i.e. $\Delta y_{max} = \Delta z_{max} \approx 0.04R$ in the bi-polar grid. This resolution was found to be sufficient as doubling the number of points did not result in an appreciable change to the calculated POD modes and the POD energy spectrum. The POD was computed using the method of snapshots[51] from 3000 independent snapshots of the fluctuating velocity field.

Using a similar snapshot POD analysis of full-bore pipe-flow, Hellström and Smits[47] reported that the first six POD modes contain around 10 to 12% of the scaled energy. In contrast, the first six POD modes in our partially-filled pipe flow contribute between 22 to 25% of the scaled energy (see figure 7), with their respective POD mode shapes shown in figures 8, 9 and 10 for flow depths of $d/D = 44\%$, 62%, and 80%. The out-of-plane (axial) component is shown as filled contours, with red and blue regions representative of values of opposing sign (positive and negative) and white representing small values surrounding zero. The in-plane components are shown as vectors. As eigenmodes, the values of the contour levels and the length and direction of the vectors bear no physical meaning until weighted by their random co-efficients to recover velocity fields. However, the mode shapes do tell

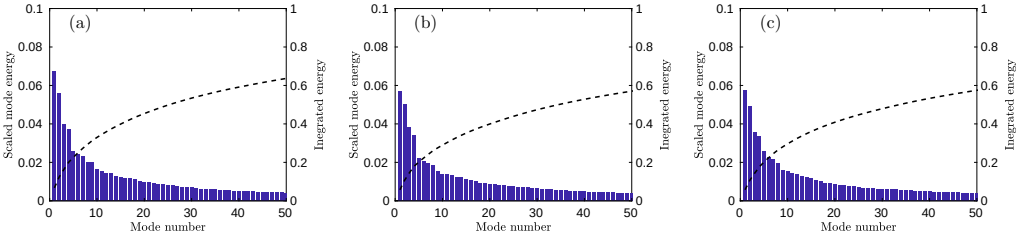

FIG. 7. Scaled energy per mode represented by blue bars and cumulative energy represented by the dashed line $(--)$, truncated to display only the first $N = 50$ modes. (a) $d/D = 44\%$, (b) $d/D = 62\%$ and (c) $d/D = 80\%$.

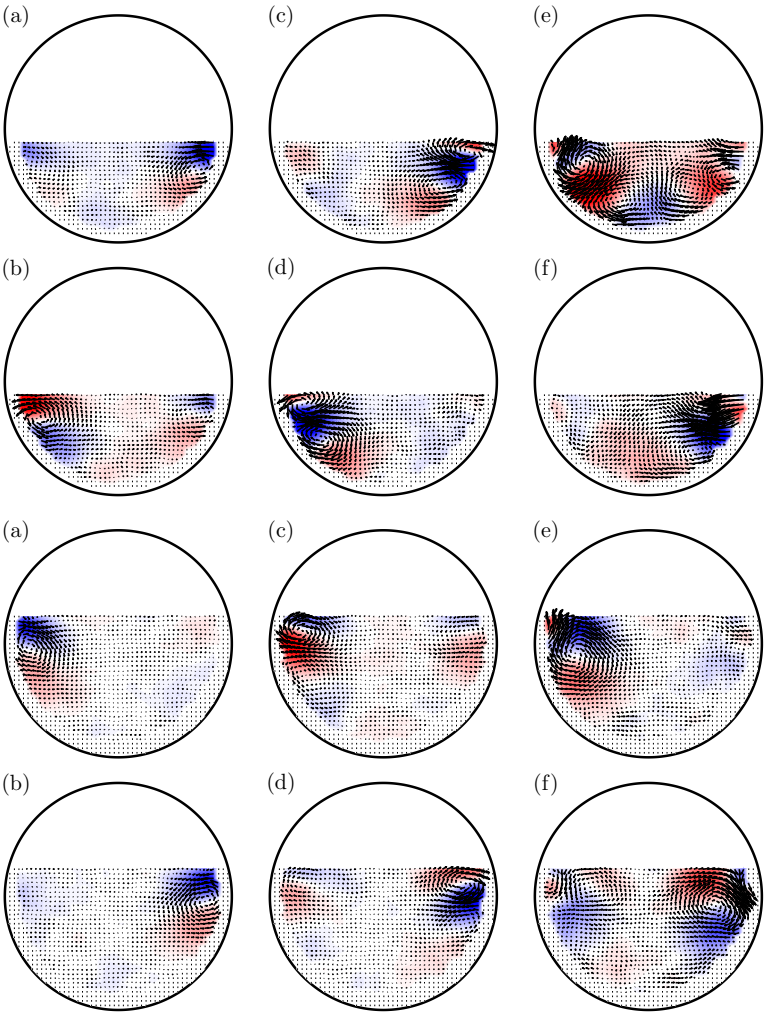

FIG. 8. The first six POD modes for $d/D = 44\%$. Color contours represent the eigenfunctions of the axial component Φ_u and vectors represent the in-plane components Φ_v and Φ_w. (a) $i = 1$, (b) $i = 2$, (c) $i = 3$, (d) $i = 4$, (e) $i = 5$ and (f) $i = 6$.

FIG. 9. The first six POD modes for $d/D = 62\%$. Color contours represent the eigenfunctions of the axial component Φ_u and vectors represent the in-plane components Φ_v and Φ_w. (a) $i = 1$, (b) $i = 2$, (c) $i = 3$, (d) $i = 4$, (e) $i = 5$ and (f) $i = 6$.

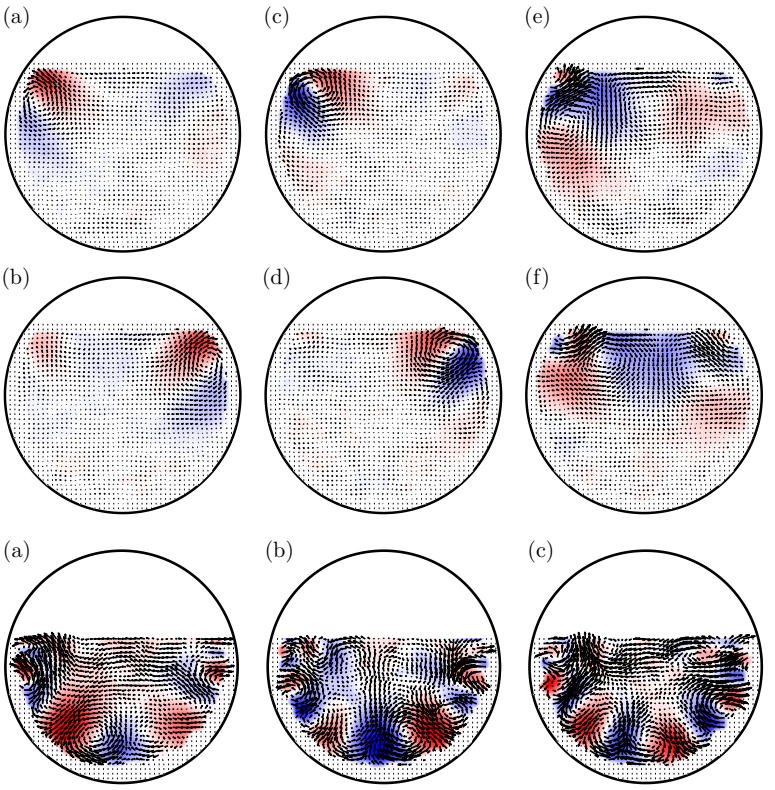

FIG. 10. The first six POD modes for $d/D = 80\%$. Color contours represent the eigenfunctions of the axial component Φ_u and vectors represent the in-plane components Φ_v and Φ_w. (a) $i = 1$, (b) $i = 2$, (c) $i = 3$, (d) $i = 4$, (e) $i = 5$ and (f) $i = 6$.

FIG. 11. Example higher order POD modes for $d/D = 62\%$. Color contours represent the eigenfunctions of the axial component Φ_u and vectors represent the in-plane components Φ_v and Φ_w. (a) $i = 20$, (b) $i = 28$ and (c) $i = 35$.

us the *location* of large-scale motions that contribute the most energy and here the contour levels and lengths of the arrows have been scaled consistently across the six modes and three flow depths to provide a like-for-like comparison.

It is clear from figures 8-10 that the energy containing motions associated with the leading order POD modes appear near the interface of the free surface and the no-slip wall, or "corner", in the partially-filled geometry. This is particularly apparent at the highest flow depth ($d/D = 80\%$) where the active parts (intense regions of blue and red) of the first four modes (figures 10a-d) are all confined to the "corner" region. These active regions are characterised by large-scale roll motions, where the core of the roll cells tracks closely with $\Phi_u \approx 0$ (which essentially means $u/U \approx 0$ i.e. traveling at the mean velocity) that we interpret are the signature of the instantaneous roll cells identified previously in partially-filled pipe flows[6] and are common to open channel flows[28,34]. We note that this signature of the instantaneous roll cells appear to be present at all flow depths tested and is the dominant feature contained in the first two POD modes for $d/D = 44\%$ (figure 8a,b) and first six POD modes for the $d/D = 62\%$ (figure 9a-f) and $d/D = 80\%$ (figure 10a-f). These low-order modes appear to come in pairs mirrored about the vertical bisector, the symmetry plane in this flow. Interestingly, the signatures representative of the large-structures that appear in the "corners" do not appear simultaneously in the same mode number. We suspect that this may be due to a combination of the large-scale instantaneous roll cells being free to grow to sizes exceeding the pipe radius, as well as, the migration of these roll cells beyond the pipe vertical bisector. At $d/D = 62\%$ and 80%, the modes $i = 5$ and $i = 6$ reveal the instantaneous signature of "upwellings" and "downdrafts" present near the corners. Upwellings and downdrafts are prominent features of free-surface turbulence and Banerjee[33] describes the former, when looking down onto the free surface, as regions on or very near the free surface where the 'streamlines radiate outwards' and the latter as regions where 'streamlines converge forming what look like lines of stagnation flow'. We suspect that the signature of upwellings and downdrafts observed in modes $i = 5$ and $i = 6$ for $d/D = 62\%$ (figure 9e,f) and $d/D = 80\%$ (figure 10e,f) are related to so-called second quadrant (Q2) and fourth quadrant (Q4) events[52] or the "burst/ejections" and "sweeps" which form the backbone of the self-sustaining mechanism of wall turbulence. Here, how-

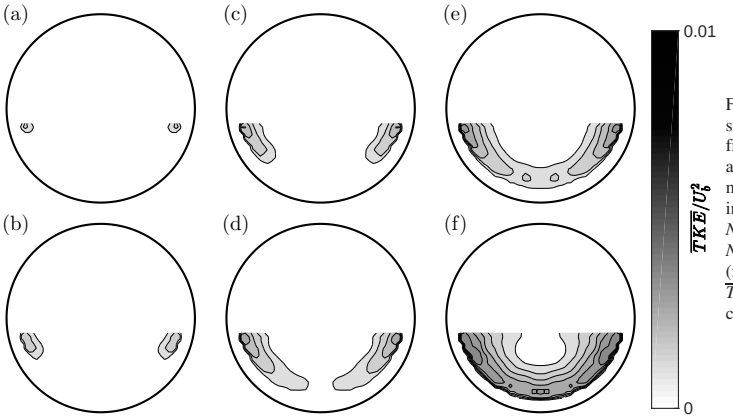

FIG. 12. Cumulative distributions of scaled energy for $d/D = 44\%$ calculated from low order representation of fluctuating velocity fields including up to N modes with cumulative energy provided in parentheses. (a) $N = 2(\approx 10\%)$, (b) $N = 4(\approx 20\%)$, (c) $N = 9(\approx 30\%)$, (d) $N = 16(\approx 40\%)$, (e) $N = 26(\approx 50\%)$ and (f) $N = 90(\approx 75\%)$. Contour levels of $\overline{TKE}/U_b^2$ vary from 0.001 to 0.01 in increments of 0.0005.

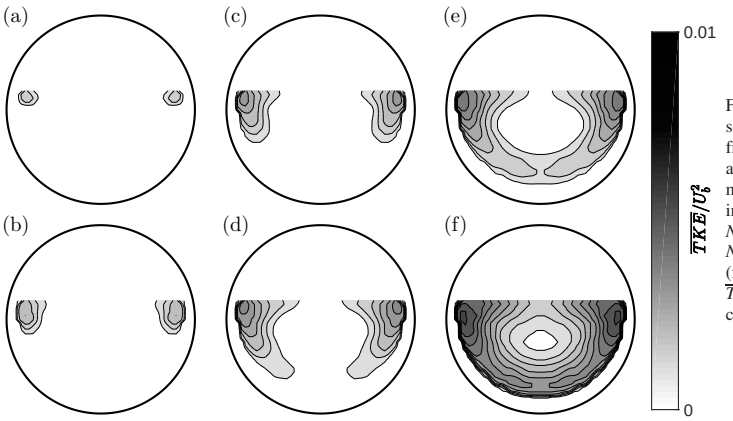

FIG. 13. Cumulative distributions of scaled energy for $d/D = 62\%$ calculated from low order representation of fluctuating velocity fields including up to N modes with cumulative energy provided in parentheses. (a) $N = 2(\approx 10\%)$, (b) $N = 5(\approx 20\%)$, (c) $N = 11(\approx 30\%)$, (d) $N = 21(\approx 40\%)$, (e) $N = 35(\approx 50\%)$ and (f) $N = 132(\approx 75\%)$. Contour levels of $\overline{TKE}/U_b^2$ vary from 0.001 to 0.01 in increments of 0.0005.

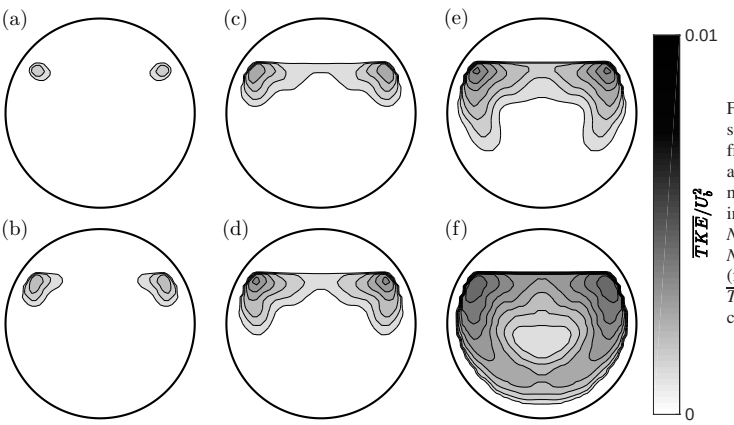

FIG. 14. Cumulative distributions of scaled energy for $d/D = 80\%$ calculated from low order representation of fluctuating velocity fields including up to N modes with cumulative energy provided in parentheses. (a) $N = 2(\approx 10\%)$, (b) $N = 5(\approx 20\%)$, (c) $N = 11(\approx 30\%)$, (d) $N = 19(\approx 40\%)$, (e) $N = 34(\approx 50\%)$ and (f) $N = 132(\approx 75\%)$. Contour levels of $\overline{TKE}/U_b^2$ vary from 0.001 to 0.01 in increments of 0.0005.

ever, the presence of the mean secondary flow changes the trajectory of the wall-normal lifting motion to a more wall-parallel motion that "lifts" fluid in the corner towards the free surface. The instantaneous signatures of upwelling and downdrafts were visualised directly from pseudo-instantaneous velocity fields in our previous work[6] where we speculated that there was a close link between upwellings or bursting motions near the corners and the instantaneous cellular structure observed near the free surface. The cause and effect of these events, however, is still an open question[53] with the bursts thought to have been *created by* the long, streamwise-oriented rolling vortices[54], as well as, vice versa[55]. Regardless of whether the bursts create the rollers or the rollers create the bursts, using POD tells us that the bursting and sweeping motions near the corner associated with the instantaneous cellular structures account for nearly a quarter of the relative energy in our turbulent partially-filled pipe flow at flow depths of $d/D = 62\%$ and 80%.

At $d/D = 44\%$, the second POD mode pair, $i = 3$ and $i = 4$ (figure 8c,d) is located slightly away from the free surface and there appears a pair of rollers which combined with the out-of-plane component is representative of negative streamwise velocity fluctuations and positive wall normal velocity fluctuations, or vice versa. In other words, these modes provide a more classical view of the aforementioned Q2 and Q4 events. At this flow depth in our partially-filled configuration these events also contribute to the aforementioned upwellings, downdrafts and instantaneous cellular structures due to their size (filling almost half the flow cross-sectional area) and proximity to the free surface. Only for $i = 5$ do we observe a repeating pattern of high and low Φ_u associated with vortex pairs around the perimeter of the pipe wall in a quasi-azimuthally-periodic arrangement.

In fully-developed canonical pipe flow, the flow is periodic in the streamwise and azimuthal directions, thus the basis functions, or POD modes, are known and can be prescribed *a priori* in a classical POD analysis. Using classical POD, it has been shown that the leading order POD modes have a radial mode number of $i_r = 1$[14,49] and azimuthal mode numbers of $i_\theta = 2$ and $i_\theta = 3$ which were identified with the large- and very-large-scale motions. When $i_r = 1$, the POD modes are interpreted as representative of wall-attached motions. These eigenmodes fill a large proportion of the pipe cross-section, are characterized by azimuthally-alternating regions of positive and negative Φ_u and become larger (both taller and wider) with smaller azimuthal wavenumber. In a partially-filled pipe, the mode shapes are not prescribed and we observe vastly different behaviour. The leading-order modes are confined to the corner regions and contribute a signficant amount of the scaled energy, however, azimuthally-alternating regions of positive and negative Φ_u emerge at higher-order modes (figure 11). For illustrative purposes we only show the $d/D = 62\%$ flow (with $d/D = 44\%$ and $d/D = 80\%$ omitted for brevity) and plot in figure 11 a selected number of higher-order modes $i = 20$, 28 and 35. These modes reveal a distinct arrangement of quasi-azimuthally-periodic, wall-attached motions where the most active portions are largely confined to the perimeter around the pipe wall. These wall-attached motions feature regions of positive Φ_u flanked by negative Φ_u (and vice versa) with roll pairs that are closely associated with $\Phi_u \approx 0$ which we interpret as a quasi-azimuthally-periodic signature of Q2 and Q4 motions and quasi-streamwise vortices. Importantly, as the number of roll pairs and associated patches of $+\Phi_u, -\Phi_u, +\Phi_u$ (or $-\Phi_u, +\Phi_u, -\Phi_u$) increases, they become smaller i.e. as the number of wall-attached structures increases, the wall-attached structures themselves become proportionally smaller suggesting a geometrically self-similar hierarchical behaviour. For even higher-order modes, the coherence of the structures continues to break down indicating that the energy contribution of those modes comes from the smaller-scale, less coherent, motions. Importantly, the emergence of the signature of the wall-attached modes with radial mode number $i_r = 1$ appear in POD modes of appreciably higher order in partially-filled pipe flow than in full pipe flow. This is not to say that the LSM and VLSM are no longer dominant motions but rather the wall-attached LSM and VLSM signatures near the bottom of the pipe appear to contribute less energy than those which form near the corners and populate the flow cross-section close to the free surface.

Whilst the eigenmodes or POD modes inform us of the shapes of the coherent structures, strictly, they have no physical meaning until combined with their temporal coefficents and projected back onto the velocity fields. Using equation 1, we reconstruct the fluctuating velocity fields up to N^{th} order, where $N = N_{max}$ will recover the full fluctuating velocity field. In this way, the POD acts as an inhomogeneous spatial filter, and we can generate a low-order representation of the velocity fields for $N < N_{max}$ from which we can compute the spatial *cumulative* TKE distributions by superposition of the POD filtered snapshots. These cumulative distributions of TKE (calculated over the flow cross-sectional area and then averaged about the vertical bisector to improve statistics) are shown in figures 12 to 14 for $d/D = 44\%$, 62% and 80%. When the number of modes N is gradually increased such that the cumulative TKE distributions are reconstructed from fluctuating velocity fields using modes containing up to 10, 20 and 30% of the scaled energy (figures 12a-c, 13a-c and 14a-c) the spatial distribution of the cumulative TKE remains confined to the corner regions in close proximity to the free surface for all three flow depths. For $d/D = 44\%$ the cumulative TKE field begins to fill the bottom region of the pipe for $N = 16$ modes corresponding to the first 40% of the scaled energy (figure 12d) and only when the low-order representation takes into account the first $N = 26$ modes and 50% of the scaled energy (figure 12e) does the distribution close up into a single band around the azimuth of the pipe wall. The behaviour of the cumulative energy distribution is similar for $d/D = 62\%$. Up to the first 30% of the scaled energy resides close to the free surface near the corner region, but when including all modes up to $N = 22$ that contain the first 40% of the scaled energy (figure 13d), we see the cumulative TKE distribution spread towards the bottom of the pipe and by including modes up to $N = 38$ (the first 50% of the scaled energy) the cumulative TKE distribution emerges at the bottom of the pipe (figure 13e). In this distribution, and those that contain the first 75% of the scaled energy (figure 13f), we see that the cumulative

TKE persists near the free surface and grows from the corner region towards the pipe vertical bisector. At $d/D = 80\%$, even when using modes that contain up to 50% of the scaled energy (figure 14e), the cumulative TKE distribution is confined to the top half of the flow cross sectional area in close proximity to the free surface. Including higher-order modes up to $N = 132$, the POD-filtered fluctuating velocity field contains 75% of the scaled energy and the cumulative TKE distribution for this case (figure 13f) reveals appreciable contributions at the bottom of the pipe.

Using snapshot POD on the fluctuating velocity field, we have shown that around 20 to 25% of the energy is captured in the first six modes for each flow depth investigated. Importantly, these energy containing motions are confined close to the corner where the free surface meets the no-slip wall. The signatures of large-scale wall-attached motions appear in higher-order modes as opposed to full pipe flow where they dominate the very first few modes. That the first $N = 6$ modes contribute almost a quarter of the scaled energy in partially-filled pipe flow, as opposed to around 12% in a full pipe flow[47], suggests that the large-scale structures that populate the "corners" are more energetic than their wall-attached counterparts that populate the near-wall regions away from the free surface. We hypothesize that this is due to the coupling and interaction of the large-scale motions with the mean secondary flow and free surface, both absent in canonical pipe flow. The free-surface, which is a shear-free and impermeable boundary allows the growth of the large-scale motions that form near the "corners" whilst at the same time the mean secondary flow sweeps these motions away from the wall along laterally, i.e. along the free surface, forming so-called instantaneous roll cells. The presence of the free surface also breaks azimuthal symmetry, hence the low order modes in partially filled pipes are not confined to ordered pairs that appear periodically around the pipe azimuth as in full pipe flow[14,47,49]. This migration of the large-scale motions and their coupling with the mean secondary flow may explain why fewer POD modes are needed to account for a larger proportion of the scaled energy when compared to full pipe flow. Conceptually, this appears to be supported by the cumulative spatial TKE distributions calculated from POD-filtered fluctuating velocity fields which show that the energy containing motions for up to the first 30% of the total relative energy resides near the free surface at flow depths of $d/D = 44\%$ and $d/D = 62\%$, with this proportion increasing to the first 50% for a flow depth of $d/D = 80\%$.

V. DISTRIBUTION OF LARGE STRUCTURES

Snapshot POD has allowed us to visualize the location and infer the makeup of the scales of motions that contribute the most energy and from the POD filtered velocity fields we reveal that anywhere between 30 to 50% of the scaled energy resides in the upper part of the flow cross-sectional area in close proximity to the free surface. We conjecture that the low-order POD modes contain the signature of the formation and evolution of instantaneous cellular structure and that these very-large-scale roll cells contribute a large proportion of the TKE, as borne out in the cumulative distributions. Now we attempt to elucidate a link between the instantaneous cellular structure and the large- and very-large-scale motions previously observed in canonical pipe flow by determining the distribution of these large-scale structures from instantaneous flow fields. Figures 15(a,c,e) presents example snapshots of pseudo-instantaneous streamwise velocity fluctuations for flow depths of $d/D = 44\%$, 62% and 80%. These snapshots were reconstructed from the high-speed S-PIV data (see: table I) using Taylor's[56] frozen turbulence approximation with the convection velocity taken to be U_b. Whilst Taylor's hypothesis has been shown to be a valid estimate for projecting temporal information into the spatial domain, choosing the 'correct' convection velocity in this flow configuration is particularly challenging as the mean streamwise velocity in partially filled pipes is distorted relative to a full pipe flow and therefore the ratio of bulk velocity to local mean velocity is a function of both radial *and* azimuthal position. We have, therefore, chosen the bulk velocity U_b as the convection velocity out of convenience and acknowledge that this can lead to an over/underestimation of the structure pseudo-lengths. Thus, we essentially limit ourselves only to a *qualitative* comparison of structure lengths and spatial distributions across flow depths, where we have used Taylor's hypothesis to infer spatial information from the planar S-PIV measurements.

Since our primary interest is the large-scale coherent structures, a moving average filter with kernel size $0.12 \times 0.12 \times 1R$ (elongated in the streamwise direction) was applied to the snapshots to remove small scale velocity fluctuations and S-PIV noise. We have selected an isosurface threshold level of $\pm 10\%$ of the local mean velocity, i.e.

$$u_{iso} = \pm 0.1U \tag{4}$$

where low-speed events are shown in blue isosurfaces and high speed events in red. This threshold value has been used in previous studies[14,19,57] and allows us to clearly demarcate between low- and high-speed structures with clear separation from the local mean velocity. Figure 15 reveals the presence of long, streamwise aligned streaky structure characterized by streamwise velocity fluctuations alternating from positive-negative-positive (or vice versa) and with lengths $O(10R)$ which are the instantaneous signature of the large- and very-large-scale motions (LSM/VLSMs) in pipe flows first reported by Kim and Adrian[7]. These LSM and VLSM scale events (also known as "Superstructures" in turbulent boundary layers) are well documented for canonical wall-bounded turbulent flows using both experimental[8,9,11] and numerical approaches[13,17,57].

From the filtered pseudo-instantaneous fields of streamwise velocity fluctuations, we compute the isosurfaces with a threshold level corresponding to equation (4). Individual large-scale structures are then identified as the "connected" regions in the isosurfaces from which we can determine the "spines" of the individual structures (the geometric center of the individual connected isosurface regions). We define a non-dimensional streamwise pseudo-length-scale as $\Delta x^* = \Delta T U_b / R$ where we have chosen R as the length scale to fa-

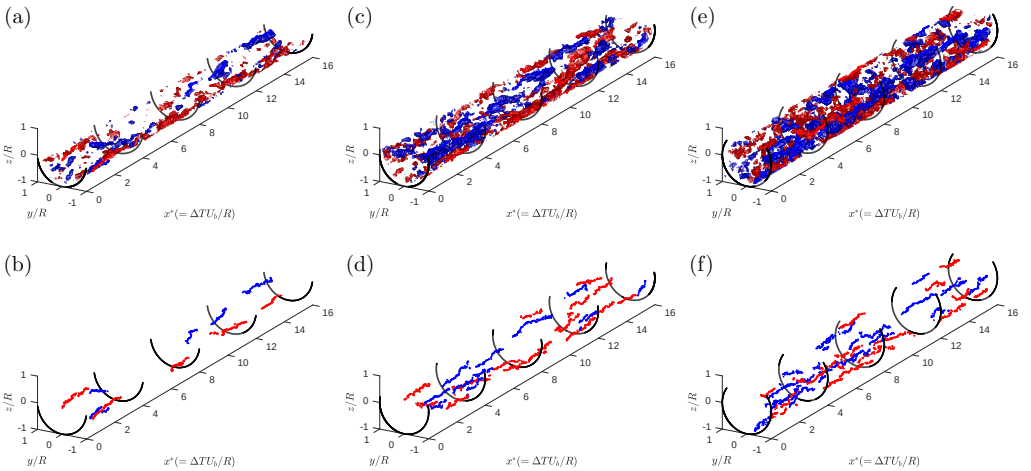

FIG. 15. Pseudo-instantaneous snapshots of streamwise velocity fluctuation at flow depths (a) $d/D = 44\%$, (c) $d/D = 62\%$ and (e) $d/D = 80\%$. Isosurface levels of $u_{iso} = \pm 0.1U$ with low-speed events displayed in blue and high-speed events in red. "Spines" of the isosurfaces or discrete large-scale events for $\Delta TU_b/R > 1$ corresponding to (a,c,e) shown in (b,d,f).

cilitate direct comparison to canonical pipe flow. To further emphasize our interest in the large-scale structures, we discard identified structures that are $\Delta x^* < 1$ in length. Figures 15(b,d,f) shows the "spines" corresponding to the filtered pseudo-instantaneous velocity fields shown in figure 15(a,c,e). We see here that in partially-filled pipe flow the instantaneous signatures of large-scale structures found in canonical wall bounded turbulent flows remain, albeit appearing less frequently as the flow depth decreases. The number of large-scale structures appears to decrease monotonically with decreasing flow depth in figure 15 and this becomes clear when we tally the total number of such events detected for the entire high-speed S-PIV dataset reported in table II. Further, we count more low-speed large-scale events than high-speed large-scale events, which is commensurate with past work on canonical wall-turbuence, e.g. Dennis and Nickels [19]. We also briefly consider a streamwise pseudo-length $\Delta TU_b/R_H$ based on hydraulic radius R_H (which is used as a length-scale in compound open channel flow). Again, as our focus is on large-scale structures, we discard structures identified with lengths less than $\Delta TU_b/R_H < 1$. With streamwise pseudo-length defined as $\Delta TU_b/R_H$, the total number of detected large-scale structures ($\Delta TU_b/R_H > 1$) increases, as expected, because with $R_H/R < 1$ (as it is for all flow depths considered here) we are excluding less of the "smaller" events. Even when changing the length-scale to R_H the number of low-speed events remains larger than the number of high-speed events (see table II).

Now that the large-scale structures have been identified we can calculate the distribution of their lengths for different flow depths. Structure lengths are estimated by subtracting the axial location of the most downstream "spine" point from the axial location of the most upstream "spine" point for each of the individual "spines". With this type of analysis, structure characteristics will depend on the isosurface threshold level used to define the structures, however, as our main interest here is to obtain a *distribution* of structure lengths rather than exact values, these limitations in the methodology will not affect the conclusions. Further, to compare population densities across flow depths and different numbers of PIV realisations, we scale the number of events detected, n, by "flow volume", $(A \times TU_b)$. Here, the flow cross-sectional area, A, is multiplied by TU_b, where measurement time T is converted to a pseudo-length using Taylor's approximation with U_b as convection velocity such that the number of events per unit volume is $nR^3/(A \times TU_b)$ and $nR_H^3/(A \times TU_b)$, where R^3 and R_H^3 make the volumes dimensionless. Histograms showing the number of large-scale structures per unit volume binned according to length are shown in figure 16. We see that the number of low-speed LSMs ($1 \leq \Delta x^* \leq 3$) per unit volume scaled with pipe radius, $nR^3/(A \times TU_b)$, is fairly insensitive to changes in flow depth (figure 16a) and that there is a clearly a larger number of VLSMs at higher fill-depths for structure lengths $3 \leq \Delta x^* \leq 7$. Beyond $\Delta x^* = 7$, the distribution becomes fairly uniform, however, these very-long structures are also very rare with only one, two and five events detected for $d/D = 44\%$, 62% and 80%, respectively. The distribution of high-speed events per unit volume scaled with pipe radius (figure 16b) follows a similar trend with a larger number of VLSM-scale structures for the higher flow depths, but now no high-speed events are detected for $\Delta x^* > 4$ at $d/D = 44\%$ with only three total events detected for $\Delta x^* > 7$ over both sets of data at $d/D = 62\%$ and 80%. Large-scale structures detected when streamwise

	n structures detected for length $\Delta x^* > 1$						n structures detected for length $\Delta TU_b/R_H$					
	Low speed			High speed			Low speed			High speed		
d/D[%]	All	$1 \leq \Delta x^* \leq 3$	$\Delta x^* > 3$	All	$1 \leq \Delta x^* \leq 3$	$\Delta x^* > 3$	All	$1 \leq \Delta TU_b/R_H \leq 3$	$\Delta TU_b/R_H > 3$	All	$1 \leq \Delta TU_b/R_H \leq 3$	$\Delta TU_b/R_H > 3$
44	188	160	28	155	143	12	1176	1020	156	939	834	105
62	343	246	97	317	267	50	1267	1023	244	1080	899	181
80	447	339	108	388	308	80	1594	1340	254	1291	1060	231

TABLE II. Left: Number of structures n detected for $\Delta x^* = \Delta TU_b/R > 1$. Right: Number of structures n detected for $\Delta TU_b/R_H > 1$. Structures are broken down into those of pseudo-length between $1 \leq \Delta x^* \leq 3$ (and $1 < \Delta TU_b/R_H \leq 3$) and those exceeding $\Delta x^* > 3$ (and $\Delta TU_b/R_H > 3$).

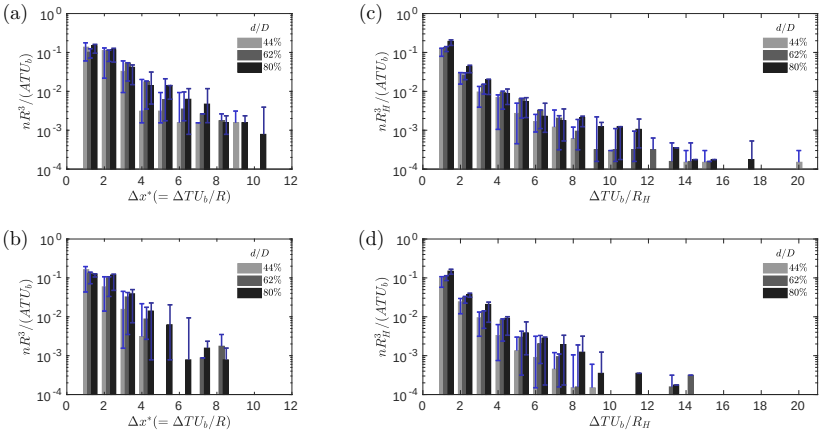

FIG. 16. Distribution of streamwise length of large-scale structures per unit volume (identified for $u_{iso} = 0.1U$) in partially-filled pipe flow for (a,c) low-speed and (b,d) high-speed. Panels (a,b) are scaled using pipe radius R and panels (c,d) are scaled using hydraulic radius R_H. Distributions colored by flow depth. Sensitivity of the computed distributions to the isosurface level shown as blue error bars which represent limits of $u_{iso} = 0.08U$ and $u_{iso} = 0.12U$.

pseudo-length is non-dimensionalised with hydraulic radius (i.e. $\Delta TU_b/R_H$) yielded histograms of $nR_H^3/(A \times TU_b)$ where the abscissa is stretched due to R_H decreasing with flow depth. The distribution of these low-speed events (figure 16c) reveals that there are, generally speaking, more LSMs and VLSMs at $d/D = 80\%$ than at $d/D = 44\%$ and 62%, although a larger number of structures were detected for $4 \leq \Delta TU_b/R_H \leq 7$ at $d/D = 62\%$. For structure lengths $8 \leq \Delta TU_b/R_H \leq 13$, there are an appreciably greater number of events for $d/D = 80\%$. The long tail in the distribution is made up of extremely rare events with only eight total events detected for $\Delta TU_b/R_H \geq 14$ over all flow depths. Scaled using hydraulic radius, the number of high-speed events per unit volume (figure 16d) decreases monotonically with flow depth, with no events registered for $\Delta TU_b/R_H > 9$ at $d/D = 44\%$ and no registered at all for $\Delta TU_b/R_H > 14$. Therefore, we find that when the number of events is weighted by "flow volume", the population of low-speed events is greater than that of the high-speed events and also tends to longer lengths, regardless of the length-scale used for normalization. Further, we find that, generally speaking, the populations of both low- and high-speed events decrease with decreasing flow depth, even when weighted by volume, suggesting a change in statistical characteristics of the large-scale structures is not simply explained by a reduction in flow area. To test the robustness of these observations, population densities were also computed with large-scale structures identified using additional thresholds of $u_{iso} = 0.08U$ and $u_{iso} = 0.12U$ (shown as error bars in figure 16). These computed distributions do reveal some sensitivity to the thresholds employed, with more events skewed towards the tails of the histograms at lower thresholds as expected. Hence, we note that estimates of the structures lengths given in this paper are for the contour level chosen ($u_{iso} = 0.1U$) and will depend on this level. However, we find that when comparing across flow depths at the same threshold level, the general trends for the distributions of structure lengths remains mostly unaffected. Thus, the conclusions of the paper will not change for isosurface threshold levels between $0.08 < u_{iso}/U < 0.12$.

We now estimate the *spatial* distribution of the large-scale structures by binning them according to their location in the r-θ plane of the pipe. First we divide the field-of-view of the S-PIV domain into a 20×20 grid, i.e. we select a bin size of $0.1 \times 0.1R$. Next, we compute the number of "spine" points that advects through each individual $0.1 \times 0.1R$ bin. Finally, we divide the "spine" points in each bin by the the total number of "spine" points which advects through the plane. Here

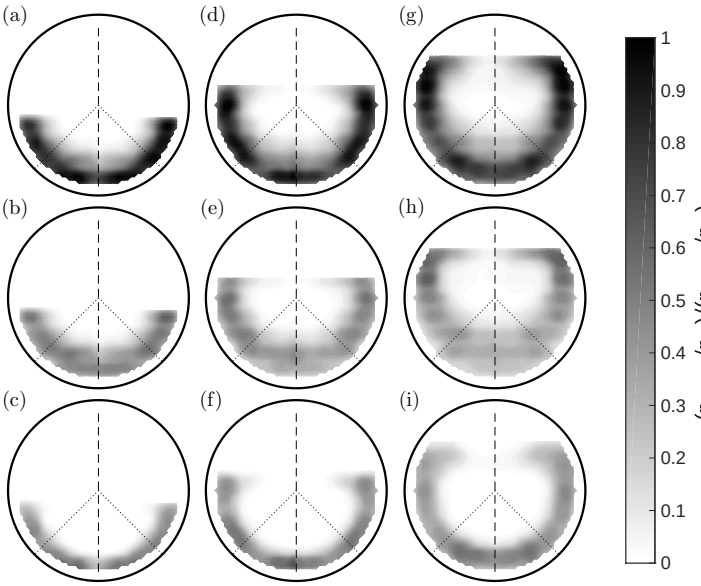

FIG. 17. Spatial distributions of the large-scale structures with streamwise pseudo-lengths $\Delta x^* > 1$ (left of bisector) and $\Delta TU_b/R_H > 1$ (right of bisector). Bin size $0.1 \times 0.1R$. Contour level indicates number of events n_{local} as a proportion of all detected events in flow cross sectional area n_{all}. Distribution of all events detected (top) and breakdown into low-speed events (middle) and high-speed events (bottom). (a-c) $d/D = 44\%$; (d-f) $d/D = 62$ and (g-i) $d/D = 80\%$. Full distributions (a,d,f) are scaled between 0 and 1 by normalizing by peak value of n_{local}/n_{all} and superposition of low-speed (b,e,h) and high-speed (c,f,i) return the full distribution. Dotted lines guide the eye to the "bottom" quadrant.

we have again considered both pipe radius R and hydraulic diameter R_H as the length-scale to non-dimensionalise the streamwise pseudo-lengths of the identified structures. The spatial distributions are calculated across the entire flow cross-sectional area and then averaged about the pipe vertical bisector (the symmetry plane in this flow) to improve the statistics. As before, only "large" scale structures are included, i.e. those with streamwise extent greater than $\Delta TU_b/R = 1$ or $\Delta TU_b/R_H = 1$. Both sets of distributions, with streamwise pseudo-lengths normalised by R and R_H, respectively, are plotted together in figure 17 with normalization by R shown on the left of the vertical bisector and normalization by R_H display on the right of the vertical bisector. In this part of the analysis we have refrained from further separating the large-scale structures into nominally LSM-scale events ($1 < \Delta TU_b/R < 3$) and VLSM-scale events ($\Delta TU_b/R > 3$) due to the relatively low number VLSM-scale events detected. Figure 17(a,d,g) shows the spatial distributions of all events detected. The contours indicate the number of events detected in the bin n_{local} divided by the total number of events detected in the flow cross sectional area n_{all} which is then scaled between zero and unity by normalising by the maximum value of n_{local}/n_{all} for each flow depth. Also shown is the breakdown into low-speed (figure 17b,e,h) and high-speed (figure 17c,f,i) structures and we note that superposition of the individual low- and high-speed distributions will recover the full distribution for each flow depth (i.e. the distribution in figure 17a = 17b+17c). Given that $R_H/R < 1$, the distributions calculated where R_H is used to non-dimensionalize streamwise pseudo-length will naturally include smaller scales which leads to subtle differences such as the distributions penetrating further into the "core" region. However, these subtle differences are small and only appreciable for $d/D = 80\%$. Therefore, the conclusions are not affected by the choice of length scale (R or R_H) and the following discussion of the spatial distribution of the large-scale structures essentially applies equally to both.

Unlike full pipe flow, where the population densities of the large-scale structures identified from instantaneous fields is only a function of wall distance[57], spatial distributions of the large-scale structures for partially-filled pipe flow exhibit an azimuthal variation due to the breaking of azimuthal symmetry. When considering the spatial distributions for all (both low- and high-speed) large-scale structures (figures 17a,d,g) we see that at $d/D = 44\%$ the distribution of the structures appears more or less uniform in the azimuthal direction whereas for flow depths $d/D = 62\%$ and 80%, the structures favor the "sides" of the pipe, close to the free surface, and the bottom quadrant of the pipe with a slight decrease in frequency near the 45° bisectors. This distribution bears a strong resemblance to the TKE distribution in figure 5, with the key difference being that the spatial distributions of the large-scale structures have sizable areas where no events greater than $\Delta x^* > 1$ (or $\Delta TU_b/R_H > 1$) are detected, suggesting that it is the increased presence of the LSM and VLSM at the "sides" and "bottom" of the pipe that are responsible for the relative increase in TKE in those regions and that it is the small scales that contribute to TKE near the core region corresponding with the "velocity dip" (figure 3). That the large-scale structures, particularly at $d/D = 62\%$ (figure 17d) and 80% (figure 17g) have a preference for the upper portion of the domain corroborates the snapshot POD where we have seen that the energy containing motions in the low-order POD modes populate the cor-

ners and flow regions close to the free surface. Further, these spatial distributions tells us that the large-scale structures also occupy the region near the vertical bisector close to the free surface (at least for $d/D = 62\%$ and $d/D = 80\%$). Thus, we surmise that there is a strong link between the LSM/VLSMs and the formation and evolution of the instantaneous cellular structures observed previously. Separating the spatial distribution of large-scale structures into low-speed (figures 17b,e,h) and high-speed events (figures 17c,f,i) it is apparent that low-speed events near the bottom of the pipe penetrate much further towards the "core" of the flow than the high-speed events which remain much closer the the pipe wall. Around the azimuth, away from the free surface (see for example the bottom quadrant in figure 17h), this is explained by the self-sustaining mechanism of wall turbulence, where axial vorticity is positively signed on the right of a low-momentum zone and negatively signed on the left of the low-momentum zone, with the converse true for the high-momentum zones. These counter-rotating vortices work together to lift low-momentum fluid from the wall and propel high-momentum fluid towards the wall in the so-called "bursts" and "sweeps" or Q2 and Q4 motions which we alluded to earlier. Near the free surface, in particular in the corners where the free surface meets the no-slip wall, the spatial distributions of the large-scale structures are compressed (as in the radial or wall-normal extent of the distribution from the corner is less than from the bottom of the pipe along the vertical bisector) which we interpret is due to the mean secondary flow changing the trajectory of the "wall-normal" bursting process (Q2), typically associated with low-speed events, to a more wall-parallel trajectory which would sweep low momentum fluid up toward the free surface (in the "corner") from which it would be transported laterally towards the pipe vertical bisector.

While the high-speed events remain closely confined to the wall for $d/D = 44\%$, with no events detected across the free surface away from the corners (figure 17c), the same is not true for the higher flow depths (figures 17f,i) and we see that high-speed events at $d/D = 80\%$ reach the pipe vertical bisector, but in only a narrow horizontal strip distinctly *below* the free surface (figures 17i), in contrast to the low-speed events which are detected in a wider horizontal band from the free surface and downwards (figure 17h). The reason for high-speed events populating a region that spans the width of the free surface for $d/D = 80\%$ is unclear but could potentially be due to lateral transport of these structures from the mean secondary flow which remains the same strength as for the $d/D = 62\%$ flow but now acts over a smaller free surface width.

The spatial distributions of the large-scale structures were also computed for isosurface threshold levels of $u_{iso} = 0.08U$ and $u_{iso} = 0.12U$ (in order the test the robustness of our observations as we did for the distributions of structure lengths). These additional spatial distributions also reveal a sensitivity to the threshold level employed with, generally speaking, more penetration of the large-scale structures into the core region of the flow for lower thresholds (due to a larger number of structures identified as "large-scale" as the threshold is reduced). Hence, we again note that estimates of the structures lengths and spatial distributions given in this paper are for the contour level chosen ($u_{iso} = 0.1U$) and will depend on this level. Importantly, however, the key trends such as the preference of the large-scale structures to populate the "corners" and "bottom" of the pipe remain unchanged with the different thresholds. Thus, the conclusions of the paper will not change (for the threshold levels considered) and we have omitted the spatial distributions computed using $u_{iso} = 0.08U$ and $u_{iso} = 0.12U$ for brevity.

By estimating the spatial distribution of the large-scale structures (with $\Delta x^* > 1$ or $\Delta T U_b/R_H > 1$) we show that the LSMs and VLSMs have a preference for the sides (in close proximity to the free surface) and bottom quadrant of the pipe for $d/D = 62\%$ and $d/D = 80\%$, whereas at $d/D = 44\%$ the flow behaves more like a shallow open channel with a curved wall. That the LSMs and VLSMs, and in particular the low-speed large-scale events, have a preference for the "corners" is consistent with the POD-filtered low-order representation of the flow field strongly suggesting that there is a dynamical link between the LSMs/VLSMs and the instantaneous cellular structures with evidence to suggest that the LSMs/VLSMs are influenced or distorted by mean secondary motion in turbulent partially-filled pipes.

VI. CONCLUSIONS

S-PIV measurements in turbulent partially-filled pipe flow have been analysed using snapshot POD, which provides an objective method to visualise the largest scale energetic motions (ranked by their energy contribution). We show that these large, energy containing structures predominantly reside in the "corner" regions where the free surface meets the pipe wall. From the shapes of two lowest-order POD modes, which reveal the presence of a single large-scale roll motion in the corner, we infer that these energetic motions are strongly connected to the instantaneous cellular structure previously observed in a wide range of open channel flows[28,53] (including our own recent work on partially-filled pipe flow[6]). The first four POD modes, all confined to the corner region in close proximity to the free surface are shown to contain approximately the first 25% of the turbulent kinetic energy for flow depths $44 \leq d/D \leq 80\%$. Using POD as an inhomogeneous spatial filter, we examine low-order reconstructions of the velocity field and compute cumulative turbulent kinetic energy distributions. The large-scale energy containing motions contribute to the overall TKE primarily in the corners, with the distribution spreading azimuthally and downwards along the pipe wall towards bottom-dead-center of the pipe when an increasingly large number of POD modes is included for the cumulative TKE distribution. At $d/D = 80\%$, however, the contribution from POD modes containing the first 50% of the scaled energy resides in the top half of the domain with the bottom of the pipe largely remaining inactive. In higher-order modes there exists the signature of azimuthally-alternating wall-attached motions (which line the pipe wall in the azimuthal direction) with very little activity in the upper portion of the domain near the free surface, indicating that the coher-

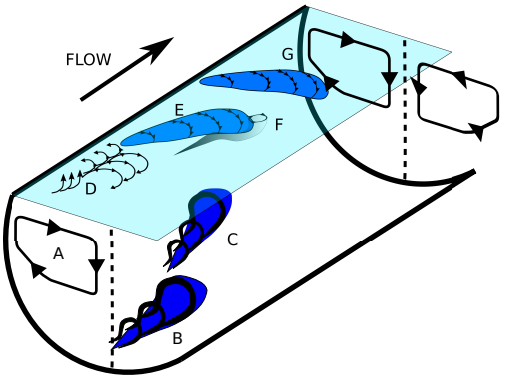

FIG. 18. Cartoon of large-scale motions in turbulent partially-filled pipe flow. (A) Mean secondary flow (shown only for one half of the geometry). (B) Large-scale (wall-attached) motions. (C) Large-scale motions influenced by mean secondary flow. (D) Bursting motion near the free surface and associated upwelling/downdraft. (E) Instantaneous roll cell. (F) Whirlpool, likely associate with hairpin/cane vortices. (G) Instantaneous roll cell swept towards vertical bisector by mean secondary flow.

ent structures of canonical wall turbulence co-exist with the dominant large-scale energetic motions associated with the free surface in turbulent partially-filled pipe flow.

Large scale structures (LSMs and VLSMs, together) identified from pseudo-instantaneous velocity fields reveal a preferential spatial distribution around the azimuth of the pipe consistent with the azimuthal variation observed in the time-averaged TKE distribution. That the LSMs and VLSMs, and in particular the low-speed large-scale events, have a predisposition for the "corners" is consistent with the POD-filtered low-order representation of the flow field strongly suggesting that there is a dynamical link between the LSMs/VLSMs and the instantaneous cellular structures in turbulent partially-filled pipes. Low-speed large-scale structures in the bottom quadrant of the pipe penetrate much further into the "core" region than the high-speed events consistent with canonical pipe flow and the classical picture of second- and fourth-quadrant events[52]. Moving around the azimuth of the pipe and towards the free surface, the spatial distributions of the low-speed events are more compressed than at the bottom of the pipe suggesting that the population density of LSMs and VLSMs are influenced by the mean secondary flow. Regardless of the link between the LSMs/VLSMs and the formation of the secondary flows, the large-scale structures that populate the region near the free surface can account for up to 30 to 50% of the TKE in turbulent partially-filled pipes.

A simple drawing summarizing the large-scale features in turbulent partially-filled pipe flow is presented in figure 18. In this cut-away view, the mean secondary flow (A) occupies the half-width of the flow cross-sectional area. The large-scale motions found in canonical pipe flow (B) appear in the partially-filled configuration and those motions that populate the bottom of the pipe are largely unaffected by the mean secondary flow (when sufficiently far from the free-surface). Moving around the pipe wall towards the free surface, the large-scale motions in full pipe flow are influenced by the mean secondary flow and swept towards the free surface (C). Bursting motions or second-quadrant events occurring in close proximity to the free surface can lead to "upwellings" and "downdrafts" (D), often found in free-surface turbulence and turbulent open channel flows. Instantaneous roll cells (E) are thought to be closely linked to the LSMs/VLSMs (B) that appear in full pipe flow, as well as, bursts that interact with the free surface (D). So-called "whirlpools" (F) also appear on the free surface which we believe are associated with "hairpin" and "cane" vortices interacting with and attaching to the free surface. Finally, the instantaneous roll cells are themselves influenced by the mean secondary flow which sweeps them towards the pipe vertical bisector and down towards the bottom of the pipe. This description of the flow features is consistent with the redistribution of the turbulent kinetic energy and appears to be supported by POD analysis and the spatial distribution of the large-scale structures presented in the manuscript.

Presently we have observed similar large-scale features to canonical pipe flow such as the LSMs and VLSMs together with the large-scale features found in open-channel flows and free surface turbulence such as instantaneous roll cells, whirlpools, upwellings and downdrafts. Our simple conceptual picture describes these large-scale features in discrete terms which is appealing, but the reality is far more complicated with evidence to suggest that all these features are dynamically linked to each other and to the observed mean secondary flow. Even with empirical evidence of these large-scale features, we do not fully understand the cause and effect of their interactions, how they scale with flow conditions and their functions. Hence, further investigation is required. There is considerable scope in this regard as the Reynolds number and Froude number scaling of even the mean flow remains largely unexplored, let alone the impact of these flow parameters on the structural composition of turbulent partially-filled pipe flow.

ACKNOWLEDGEMENTS

R.J.P. would like to thank the EPSRC for the award of a Fellowship under grant number EP/M025187/1. H.N. would like to thank Dr. Will J. H. Lee (University of Melbourne) for fruitful discussions regarding the implementation of POD. The authors would like to acknowledge the support of the National Nuclear Laboratory.

DATA AVAILABILITY

The data that support the findings of this study are available upon reasonable request.

[1]J. Guo and R. N. Meroney, "Theoretical solution for laminar flow in partially-filled pipes," J. Hydraulic Res. **51**, 408–416 (2013).
[2]A. M. J. Davis and T. Z. Mai, "Steady pressure-driven non-Newtonian flow in a partially filled pipe," J. Non-Newtonian Fluid Mech. **41**, 81–100 (1991).
[3]T. S. Ng, C. J. Lawrence, and G. F. Hewitt, "Gravity-Driven Laminar Flow in a Partially-Filled Pipe," J. Hydr. Engrg. **126**, 263–275 (2000).
[4]D. W. Knight and M. Sterling, "Boundary Shear in Circular Pipes Running Partially Full," J. Hydr. Engrg. **126**, 263–275 (2000).
[5]J. I. Yoon, J. Sung, and M. H. Lee, "Velocity profiles and friction factor coefficients in circular open channels," J. Hydraulic Res. **50**, 304–311 (2012).
[6]H. C.-H. Ng, H. L. F. Cregan, J. M. Dodds, R. J. Poole, and D. J. C. Dennis, "Partially filled pipes: experiments in laminar and turbulent flow," J. Fluid Mech. **848**, 467–507 (2018).
[7]K. C. Kim and R. J. Adrian, "Very large-scale motion in the outer layer," Phys. Fluids **11**, 417–422 (1999).
[8]N. Hutchins and I. Marusic, "Evidence of very long meandering features in the logarithmic region of turbulent boundary layers," J. Fluid Mech. **579**, 1–28 (2007).
[9]M. Guala, S. E. Hommema, and R. J. Adrian, "Large-scale and very-large-scale motions in turbulent pipe flow," J. Fluid Mech. **554**, 521–542 (2006).
[10]B. J. Balakumar and R. J. Adrian, "Large and very-large-scale motions in channel and boundary-layer flows," Phil. Trans. R. Soc. A **365**, 665–681 (2007).
[11]J. P. Monty, J. A. Stewart, R. C. Williams, and M. S. Chong, "Large-scale features in turbulent pipe and channel flows," J. Fluid Mech. **589**, 147–156 (2007).
[12]S. C. C. Bailey and A. J. Smits, "Experimental investigation of the structure of large- and very-large-scale motions in turbulent pipe flow," J. Fluid Mech. **651**, 339–356 (2010).
[13]X. Wu, J. R. Baltzer, and R. J. Adrian, "Direct simulation of a 30R long turbulent pipe flow at $R^+ = 685$: large- and very large-scale motions," J. Fluid Mech. **698**, 235–281 (2012).
[14]J. R. Baltzer, R. J. Adrian, and X. Wu, "Structural organization of large and very large scales in turbulent pipe flow simulation," J. Fluid Mech. **720**, 236–279 (2013).
[15]H. Abe, R. A. Antonia, and S. Toh, "Large-scale structures in a turbulent channel flow with a minimal streamwise flow unit," J. Fluid Mech. **850**, 733–768 (2018).
[16]J. Han, J. Hwang, M. Yoon, J. Ahn, and H. J. Sung, "Azimuthal organization of large-scale motions in a turbulent minimal pipe flow," Phys. Fluids **31**, 055113 (2019).
[17]J. H. Lee, H. J. Sung, and R. J. Adrian, "Space–time formation of very-large-scale motions in turbulent pipe flow," J. Fluid Mech. **881**, 1010–1047 (2019).
[18]B. Guerrero, M. F. Lambert, and R. C. Chin, "Extreme wall shear stress events in turbulent pipe flows: spatial characteristics of coherent motions," J. Fluid Mech. **904**, A18 (2020).
[19]D. J. C. Dennis and T. B. Nickels, "Experimental measurement of large-scale three-dimensional structures in a turbulent boundary layer. Part 2. Long structures," J. Fluid Mech. **673**, 218–244 (2011).
[20]J. H. Lee and H. J. Sung, "Comparison of very-large-scale motions of turbulent pipe and boundary layer simulations," Phys. Fluids **25**, 045103 (2014).
[21]G. Wang, H. Gu, and X. Zheng, "Large scale structures of turbulent flows in the atmospheric surface layer with and without sand," Phys. Fluids **32**, 106604 (2020).
[22]S. M. Cameron, V. I. Nikora, and M. T. Stewart, "Very-large-scale motions in rough-bed open-channel flow," J. Fluid Mech. **814**, 416–429 (2017).
[23]S. M. Cameron, V. I. Nikora, and I. Marusic, "Drag forces on a bed particle in open-channel flow: effects of pressure spatial fluctuations and very-large-scale motions," J. Fluid Mech. **863**, 494–512 (2019).
[24]D. Ferraro, F. Coscarella, and R. Gaudio, "Scales of turbulence in open-channel flows with low relative submergence," Physics of Fluids **31**, 125114 (2019).
[25]Y. Duan, Q. Chen, D. Li, and Q. Zhong, "Contributions of very large-scale motions to turbulence statistics in open channel flows," J. Fluid Mech. **892**, A3 (2020).
[26]C. Peruzzi, D. Poggi, L. Ridolfi, and C. Manes, "On the scaling of large-scale structures in smooth-bed turbulent open-channel flows," J. Fluid Mech. **889**, A1 (2020).
[27]A. Zampiron, S. Cameron, and V. Nikora, "Secondary currents and very-large-scale motions in open-channel flow over streamwise ridges," J. Fluid Mech. **887**, A17 (2020).
[28]I. Nezu, "Open-Channel Flow Turbulence and Its Research Prospect in the 21st Century," J. Hydr. Engrg. **131**, 229–246 (2005).
[29]I. Nezu and M. Sanjou, "PIV and PTV measurements in hydro-sciences with focus on turbulent open-channel flows," Journal of Hydro-environment Research **5**, 215–230 (2011).
[30]M. Rashidi, "Burst-interface interactions in free surface turbulent flows," Phys. Fluids **9**, 3485–3501 (1997).
[31]W.-T. Tsai, "A numerical study of the evolution and structure of a turbulent shear layer under a free surface," J. Fluid Mech. **354**, 239–276 (1998).
[32]S. Kumar, R. Gupta, and S. Banerjee, "An experimental investigation of the characteristics of free-surface turbulence in channel flow," Phys. Fluids **10**, 437–455 (1998).
[33]S. Banerjee, "Upwellings, downdrafts and whirlpools: Dominant structures in free surface turbulence," Appl. Mech. Rev. **47**, 166–172 (1994).
[34]K. Onitsuka and I. Nezu, "Generation mechanism of turbulence-driven secondary currents in open-channel flows," in *IUTAM Symp. on Geometry and Statistics of Turbulence*, edited by K. K. et. al. (Kluwer Academic, Boston, 2001) pp. 345–350.
[35]D. J. C. Dennis and F. M. Sogaro, "Distinct Organizational States of Fully Developed Turbulent Pipe Flow," Phys. Rev. Lett. **113**, 234501 (2014).
[36]B. E. Owolabi, D. J. C. Dennis, and R. J. Poole, "Turbulent drag reduction by polymer additives in parallel-shear flows," Journal of Fluid Mechanics **827**, R4 (2017).
[37]C. Wen, R. J. Poole, A. P. Willis, and D. J. C. Dennis, "Experimental evidence of symmetry-breaking supercritical transition in pipe flow of shear-thinning fluids," Phys. Rev. Fluids **2**, 031901 (2017).
[38]M. P. Escudier, F. Presti, and S. Smith, "Drag reduction in the turbulent pipe flow of polymers," J. Non-Newtonian Fluid Mech. **81**, 197–213 (1999).
[39]L. Prandtl, *Essentials of Fluid Dynamics* (Blackie, 1952).
[40]H. J. Perkins, "The formation of streamwise vorticity in turbulent flow," J. Fluid Mech. **44**, 721–740 (1970).
[41]G. Berkooz, P. Holmes, and J. L. Lumley, "The proper orthogonal decomposition in the analysis of turbulent flows," Annu. Rev. Fluid. Mech. **25**, 539–575 (1993).
[42]M. Tutkun and W. K. George, "Lumley decomposition of turbulent boundary layer at high Reynolds numbers," Phys. Fluids **29**, 020707 (2017).
[43]K. Taira, S. L. Brunton, S. T. M. Dawson, C. W. Rowley, T. Colonius, B. J. McKeon, O. T. Schmidt, S. Gordeyev, V. Theofilis, and L. S. Ukeiley, "Modal Analysis of Fluid Flows: An Overview," AIAA Journal **55**, 4013–4041 (2017).
[44]C. Vanderwel, A. Stroh, J. Kriegseis, B. Frohnapfel, and B. Ganapathisubramani, "The instantaneous structure of secondary flows in turbulent boundary layers," J. Fluid Mech. **862**, 845–870 (2019).
[45]S. Derebail Muralidhar, B. Podvin, L. Mathelin, and Y. Fraigneau, "Spatio-temporal proper orthogonal decomposition of turbulent channel flow," J. Fluid Mech. **864**, 614–639 (2019).
[46]H. H. Khan, S. F. Anwer, N. Hasan, and S. Sanghi, "Dynamics of coherent structures in turbulent square duct flow," Phys. Fluids **32**, 045106 (2020).
[47]L. H. O. Hellström and A. J. Smits, "The energetic motions in turbulent pipe flow," Phys. Fluids **26**, 125102 (2014).
[48]L. H. O. Hellström, I. Marusic, and A. J. Smits, "Self-similarity of the large-scale motions in a turbulent pipe flow," J. Fluid Mech. **792**, R1 (2016).
[49]J. Ahn and H. J. Sung, "Relationship between streamwise and azimuthal length scales in a turbulent pipe flow," Physics of Fluids **29**, 105112 (2017).
[50]L. I. Abreu, A. V. G. Cavalieri, P. Schlatter, R. Vinuesa, and D. S. Henningson, "Spectral proper orthogonal decomposition and resolvent analysis of near-wall coherent structures in turbulent pipe flows," J. Fluid Mech. **900**, A11 (2020).
[51]L. Sirovich, "Turbulence and the dynamics of coherent structures part i: Coherent structures," Quarterly of Applied Mathematics **45**, 561–571 (1987).
[52]J. M. Wallace, "Quadrant Analysis in Turbulence Research: History and Evolution," Ann. Rev. Fluid Mech. **48**, 131–158 (2016).
[53]R. J. Adrian and I. Marusic, "Coherent structures in flow over hydraulic engineering surfaces," J. Hydraulic Res. **50**, 451–464 (2012).
[54]A. Tamburrino and J. S. Gulliver, "Large scale structures in a turbulent open channel flow," J. Hydraulic Res. **37**, 363–380 (1999).

[55]A. B. Shvidchenko and G. Pender, "Large flow structures in a turbulent open channel flow," J. Hydraulic Res. **39**, 109–111 (2001).
[56]G. I. Taylor, "The spectrum of turbulence," Proc. R. Soc. Lond. A. **164**, 476–490 (1938).
[57]J. Lee, J. Ahn, and H. J. Sung, "Comparison of large- and very-large-scale motions in turbulent pipe and channel flows," Phys. Fluids **27**, 025101 (2015).

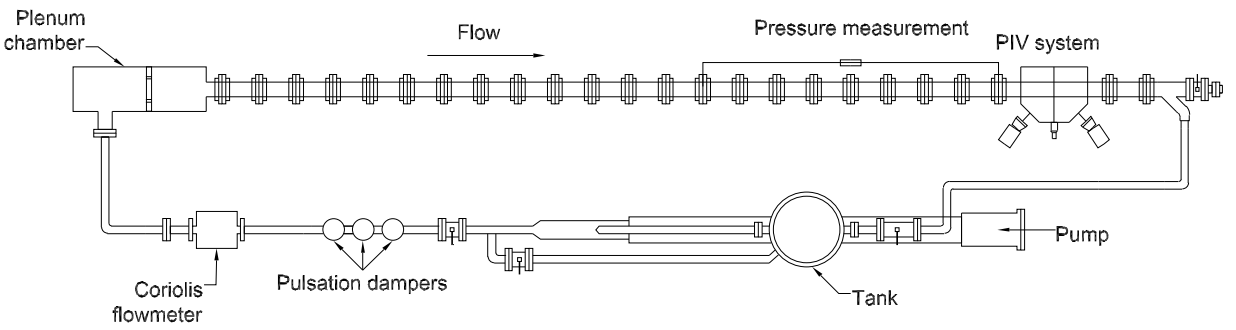

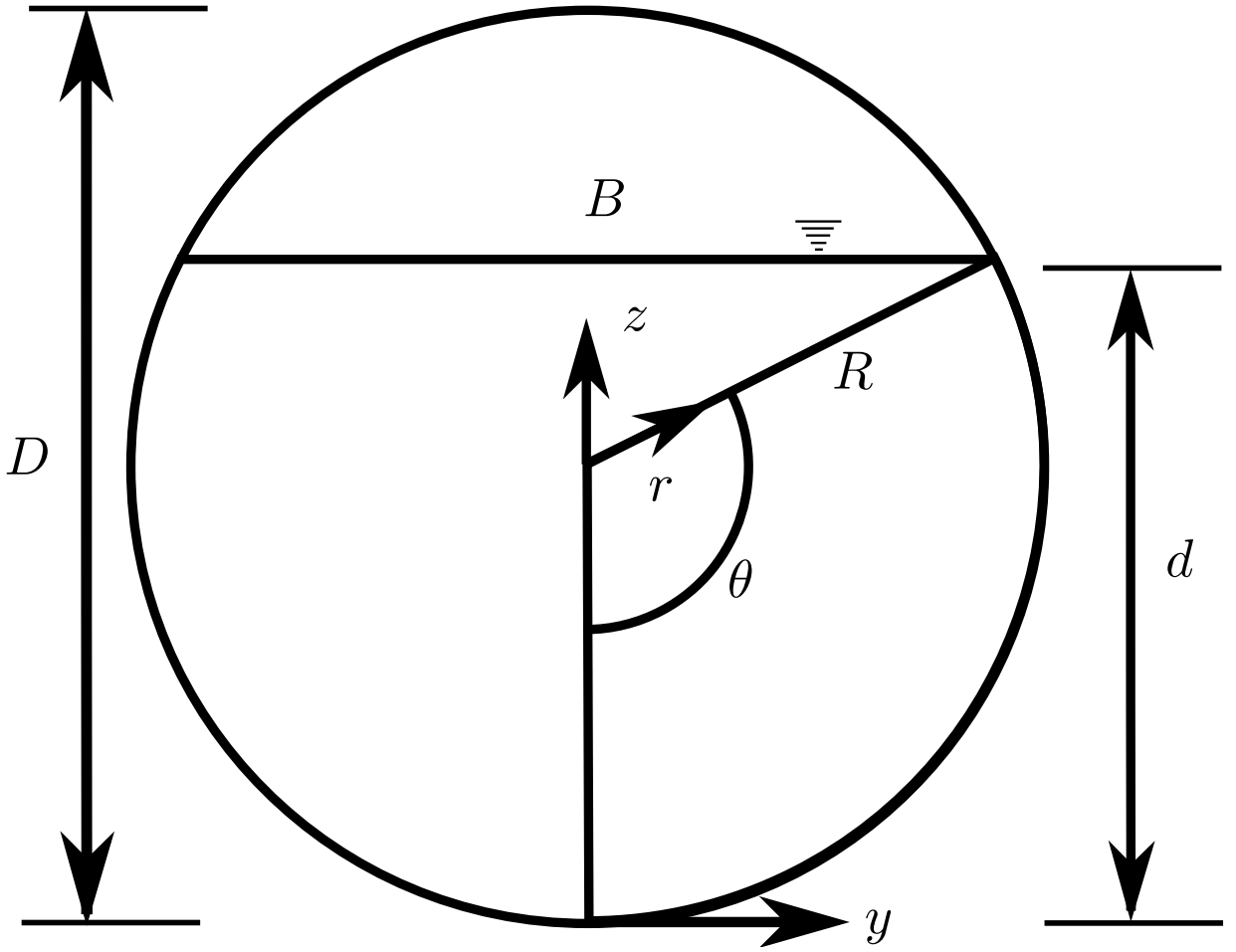

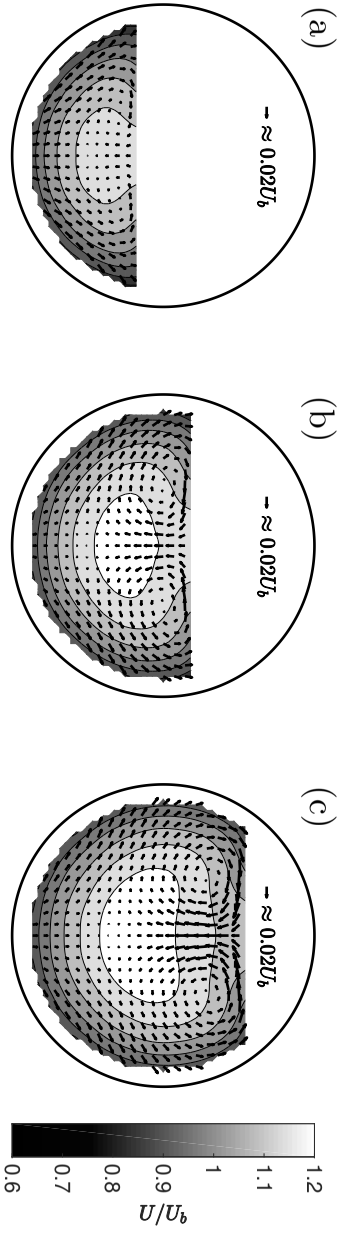

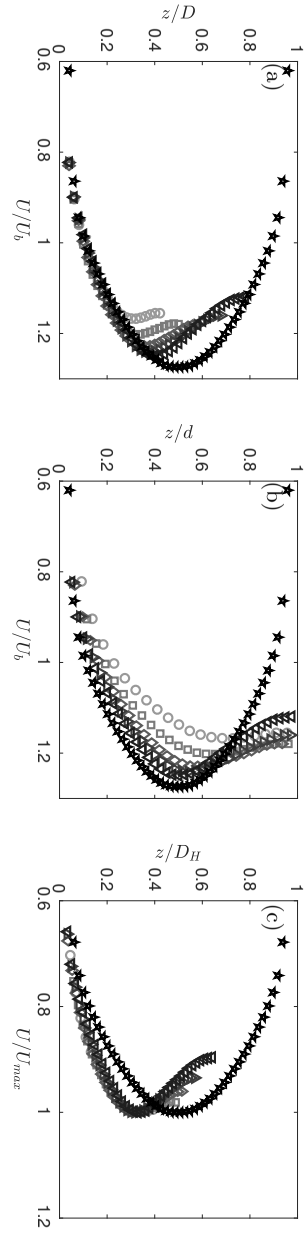

PLEASE CITE THIS ARTICLE AS DOI: 10.1063/5.0031639

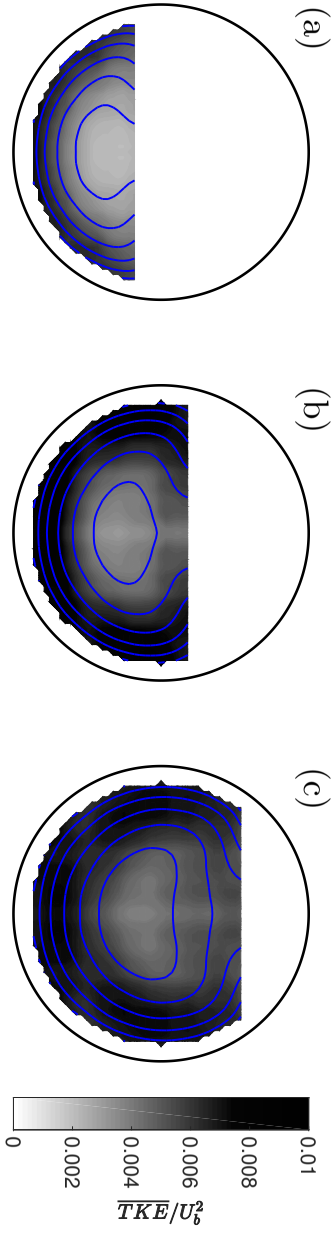

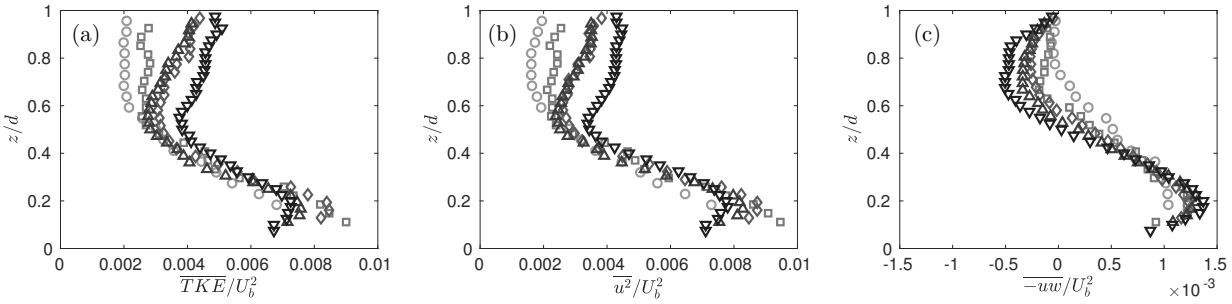

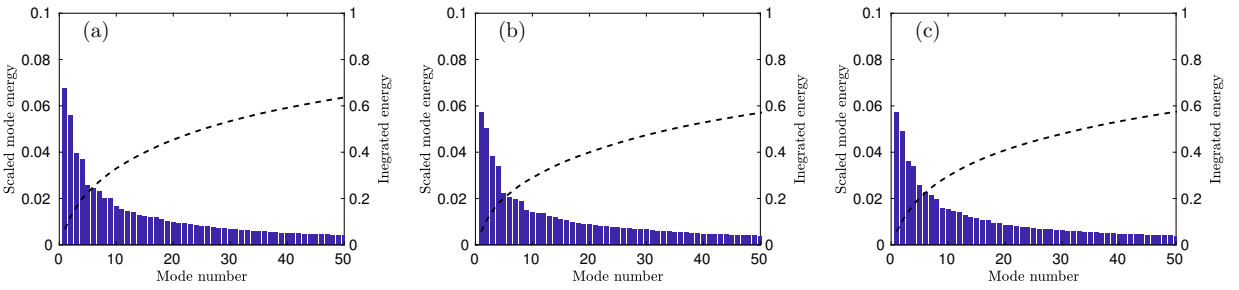

PLEASE CITE THIS ARTICLE AS DOI: 10.1063/5.0031639

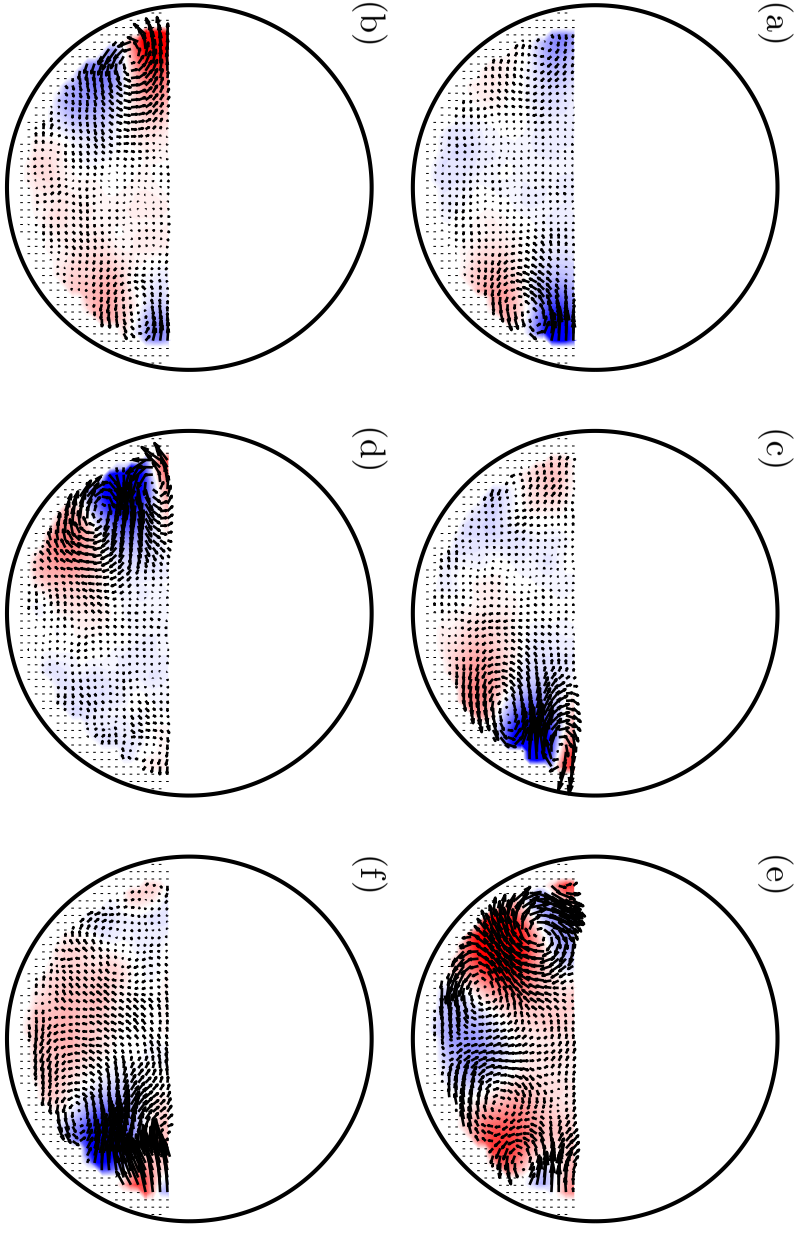

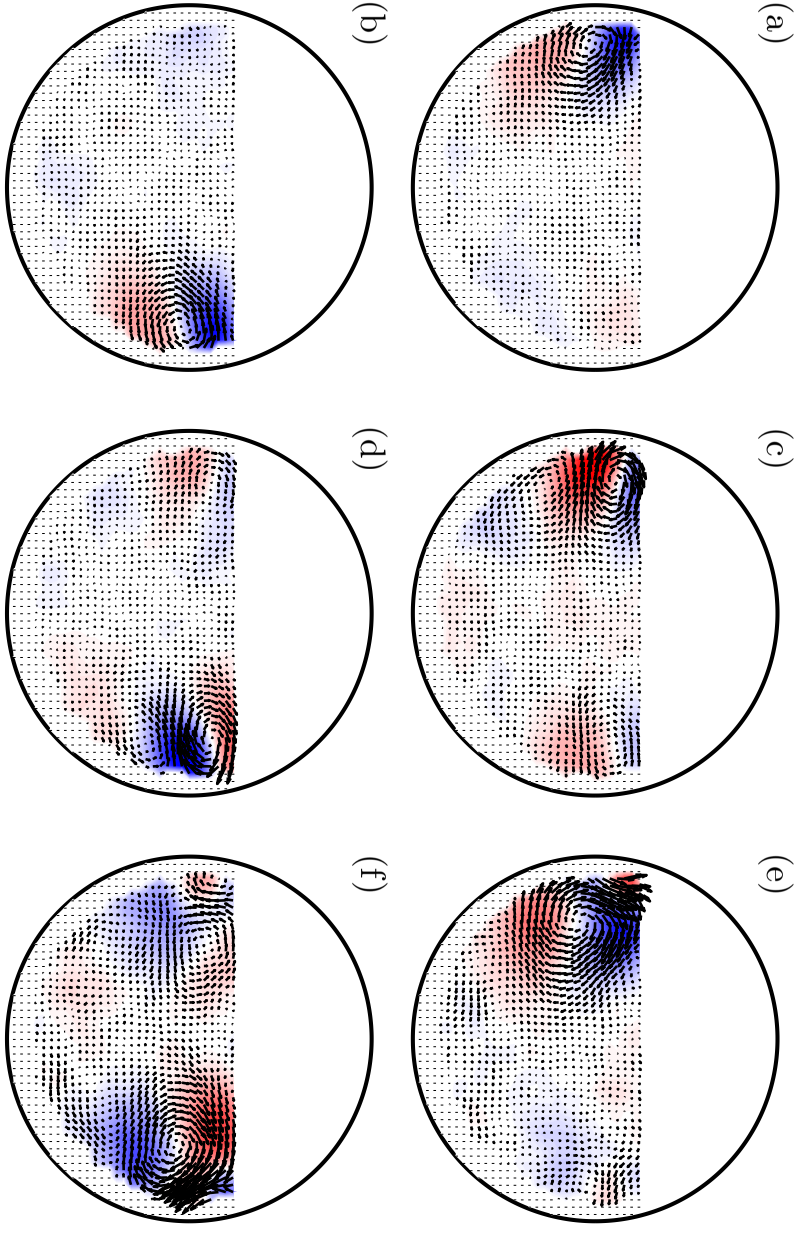

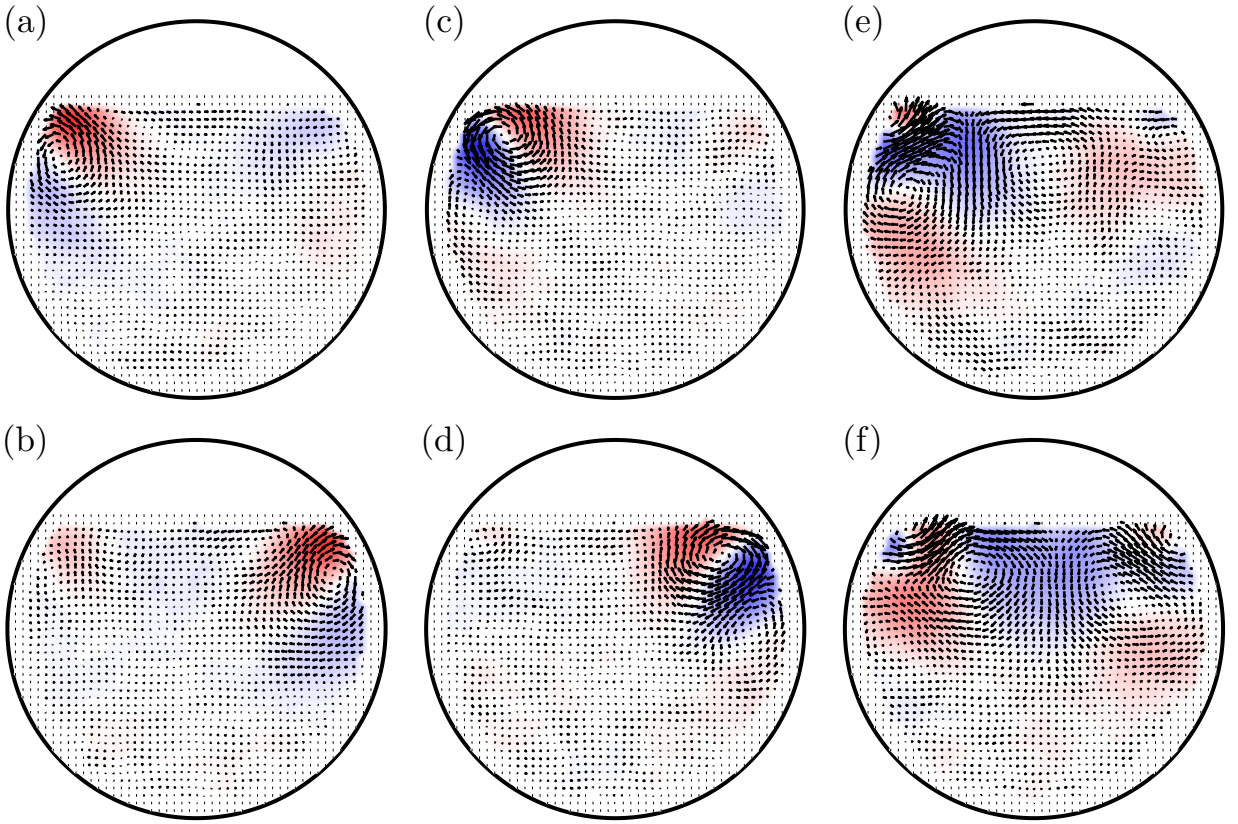

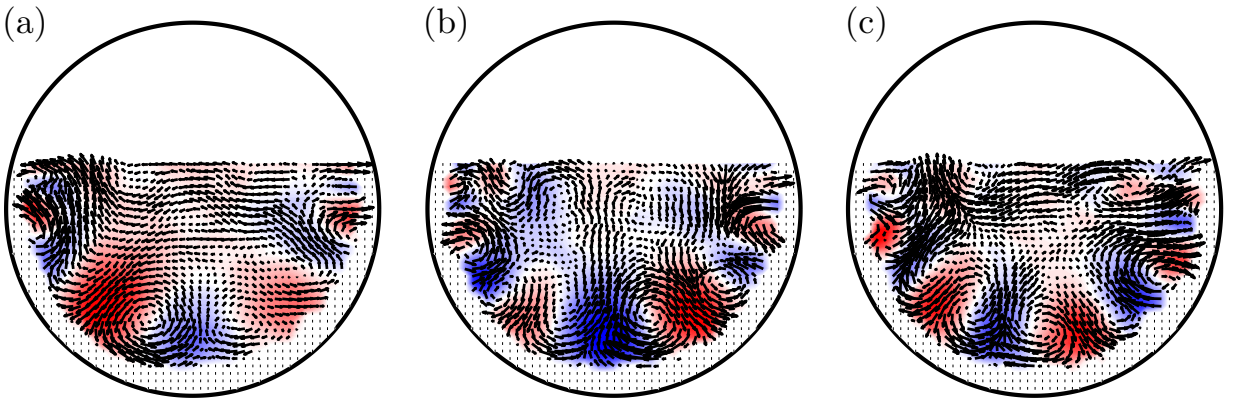

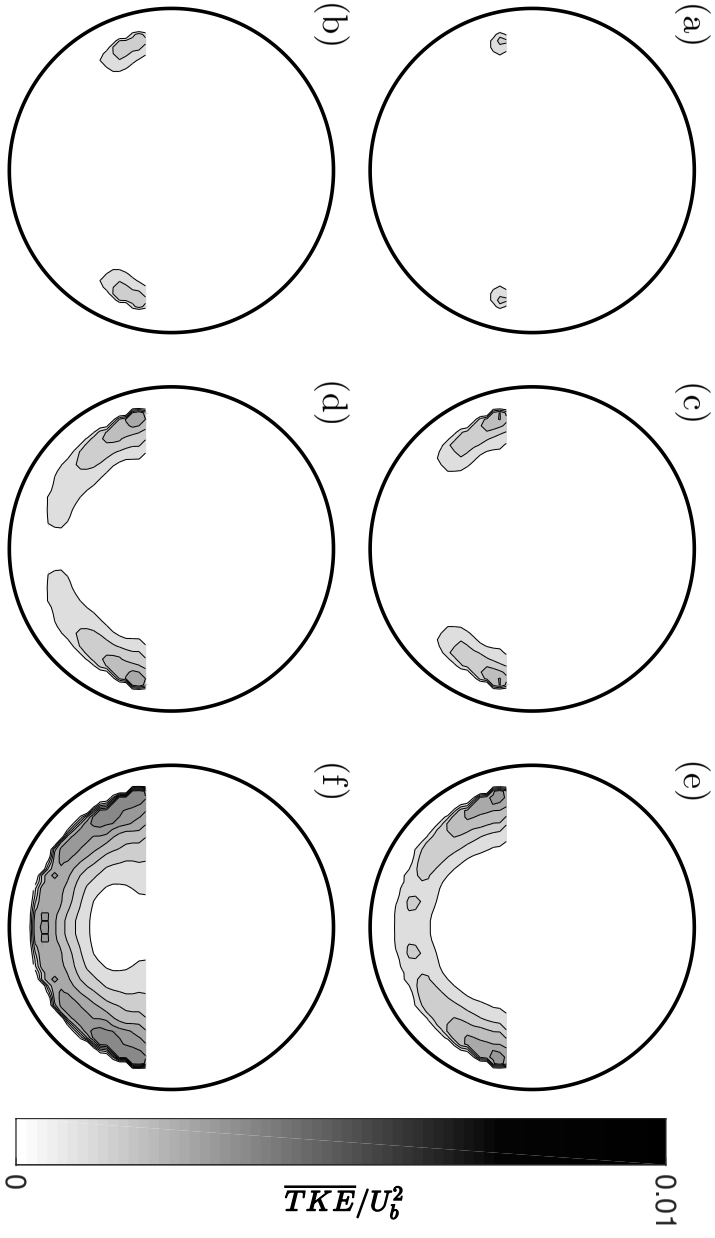

PLEASE CITE THIS ARTICLE AS DOI: 10.1063/5.0031639

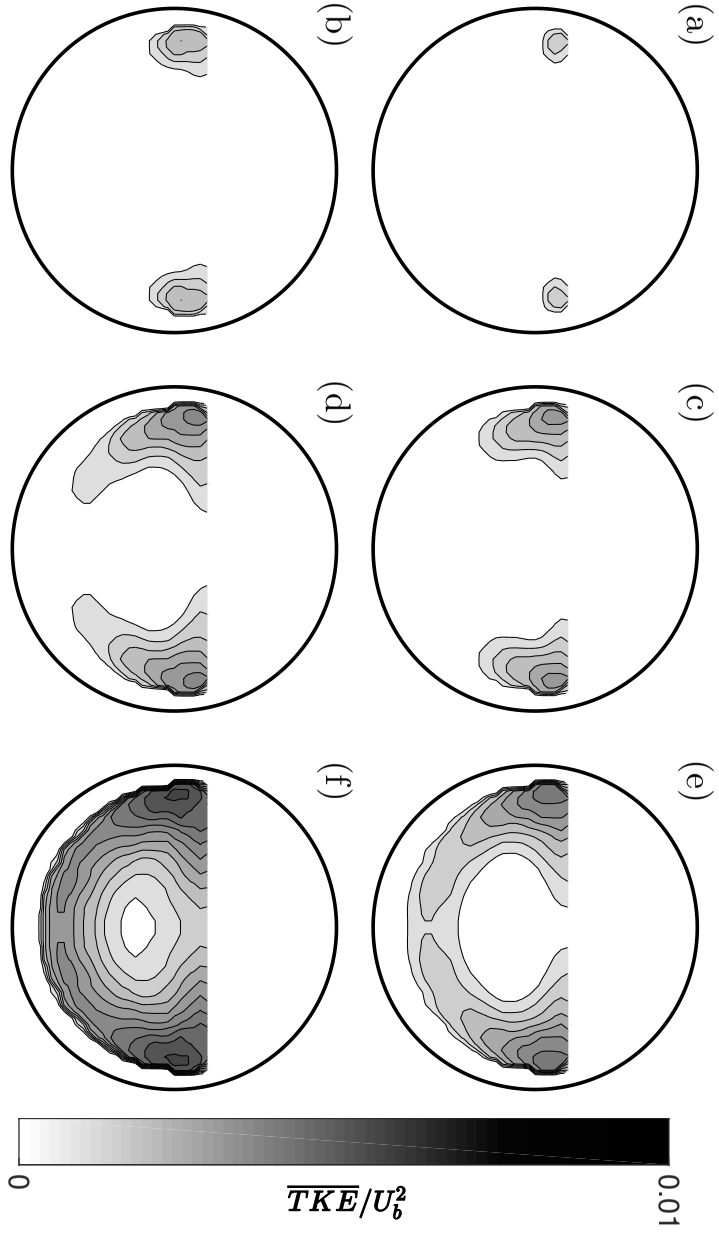

PLEASE CITE THIS ARTICLE AS DOI: 10.1063/5.0031639